Article

Cell Reports

Parallel Processing of Sound Dynamics across Mouse Auditory Cortex via Spatially Patterned Thalamic Inputs and Distinct Areal Intracortical Circuits

Graphical Abstract

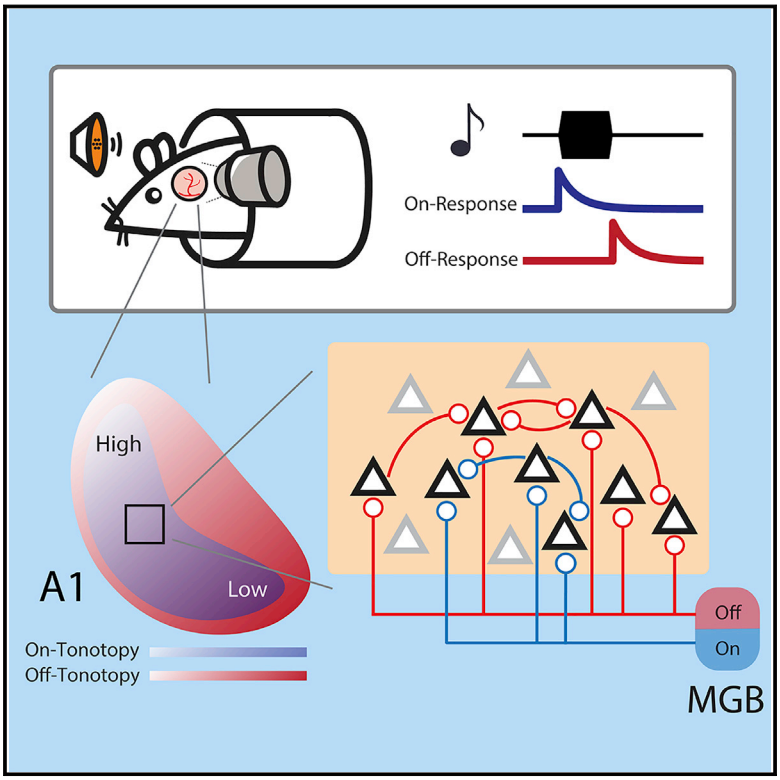

Authors

Ji Liu, Matthew R. Whiteway, Alireza Sheikhattar, Daniel A. Butts, Behtash Babadi, Patrick O. Kanold

Correspondence

pkanold@umd.edu

In Brief

Using multiscale imaging of mouse auditory cortices, Liu et al. found that the offset response is tonotopically organized and spatially extensive across auditory fields, while A1 L2/3 pyramidal neurons process tone onset and offset in parallel networks. The offset response is amplified by differential convergence of thalamic input and intracortical processing involving interneurons.

Highlights

- Automatic image segmentation defines auditory cortex fields by temporal responses
- Both onset and offset responses are tonotopically organized across auditory cortex
- Parallel neuronal networks process tone onset and offset in the auditory cortex
- A1 amplifies offset response by convergent thalamic input and intracortical processing

Liu et al., 2019, Cell Reports *27*, 872–885
April 16, 2019
https://doi.org/10.1016/j.celrep.2019.03.069

CellPress

OPEN ACCESS
CellPress

Cell Reports
Article

Parallel Processing of Sound Dynamics across Mouse Auditory Cortex via Spatially Patterned Thalamic Inputs and Distinct Areal Intracortical Circuits

Ji Liu,[1] Matthew R. Whiteway,[2] Alireza Sheikhattar,[3] Daniel A. Butts,[1,2,4] Behtash Babadi,[3] and Patrick O. Kanold[1,4,5,*]
[1]Department of Biology, University of Maryland, College Park, MD 20742, USA
[2]Applied Mathematics and Statistics and Scientific Computation Program, University of Maryland, College Park, MD 20742, USA
[3]Department of Electrical & Computer Engineering, University of Maryland, College Park, MD 20742, USA
[4]Program in Neuroscience and Cognitive Science, University of Maryland, College Park, MD 20742, USA
[5]Lead Contact
*Correspondence: pkanold@umd.edu
https://doi.org/10.1016/j.celrep.2019.03.069

SUMMARY

Natural sounds have rich spectrotemporal dynamics. Spectral information is spatially represented in the auditory cortex (ACX) via large-scale maps. However, the representation of temporal information, e.g., sound offset, is unclear. We perform multiscale imaging of neuronal and thalamic activity evoked by sound onset and offset in awake mouse ACX. ACX areas differed in onset responses (On-Rs) and offset responses (Off-Rs). Most excitatory L2/3 neurons show either On-Rs or Off-Rs, and ACX areas are characterized by differing fractions of On and Off-R neurons. Somatostatin and parvalbumin interneurons show distinct temporal dynamics, potentially amplifying Off-Rs. Functional network analysis shows that ACX areas contain distinct parallel onset and offset networks. Thalamic (MGB) terminals show either On-Rs or Off-Rs, indicating a thalamic origin of On and Off-R pathways. Thus, ACX areas spatially represent temporal features, and this representation is created by spatial convergence and co-activation of distinct MGB inputs and is refined by specific intracortical connectivity.

INTRODUCTION

Natural sounds have rich spectral and temporal dynamics, and neuronal populations along the auditory processing stream encode both spectral and temporal information. Onset (On) and offset (Off) are fundamental dynamic features of sound to which single neurons at multiple levels of the auditory system respond (He et al., 1997; Henry, 1985; Hillyard and Picton, 1978; Kopp-Scheinpflug et al., 2011), including the auditory cortex (ACX) (Baba et al., 2016; Fishman and Steinschneider, 2009; He, 2001; Qin et al., 2007; Recanzone, 2000; Scholl et al., 2010). While offset responses (Off-Rs) have been suggested to be responsible for duration coding (He, 2001), they, together with onset responses (On-Rs), encode the basic cues (On and Off) for auditory scene analysis (Bregman, 1994). Thus, besides elucidating the encoding of both sound On and sound Off, revealing the underlying cellular networks is essential for understanding auditory processing.

ACX contains multiple functional areas, and the spatial organization of ACX with respect to On-Rs has been extensively studied. On a large scale (hundreds of microns), there are clear tonotopic maps that result from topographic thalamocortical projections (Guo et al., 2012; Issa et al., 2014; Kanold et al., 2014; Merzenich et al., 1975; Stiebler et al., 1997; Tsukano et al., 2015), while on a finer scale, two-photon imaging studies in mouse primary ACX (A1) revealed a diverse tonotopic organization of On-Rs in superficial layers (Bandyopadhyay et al., 2010; Kanold et al., 2014; Rothschild et al., 2010; Winkowski and Kanold, 2013). In contrast, the spatial organization of Off-Rs in ACX is less well understood. Widefield (WF) flavoprotein imaging revealed the existence of an area adjacent to A1 that specializes in processing tone offset regardless of tone frequency in anesthetized mice (Baba et al., 2016). On a finer scale, neurons in mouse ACX show distinct On and Off-R patterns (Deneux et al., 2016), and inputs carrying On-Rs and Off-Rs are proposed to originate in nonoverlapping synaptic circuits (Scholl et al., 2010). These findings at different scales raise the possibilities that On-Rs and Off-Rs reflect distinct parallel pathways not only within A1 but also across ACX and that On-Rs and Off-Rs might be differentially represented in the cortical space. Here, we tested these hypotheses by investigating the spatial representation and functional microcircuits contributing to On-Rs and Off-Rs on multiple spatial scales in ACX.

Because multiple ACX areas contribute to auditory processing, we first performed WF imaging of GCaMP6s in awake mice. For unbiased identification of ACX areas, we developed an automated image segmentation algorithm based upon temporal responses. We detected known and other ACX areas. ACX areas differed in their response properties to tone onset and offset, indicating that temporal selectivity might underlie the auditory scene analysis in ACX. Both On-Rs and Off-Rs showed tonotopic organizations. Two-photon calcium imaging of ACX neurons revealed that most excitatory layer 2/3 neurons showed either On-Rs or Off-Rs. ACX areas were characterized by differing fractions of On-R and Off-R neurons. Parvalbumin

(PV) and somatostatin (SOM) interneurons showed differential On-R and Off-R dynamics, suggesting suppression of PV neurons by SOM neurons during prolonged tone presentations and potentially exerting a disinhibiting effect on local excitatory neurons to selectively amplify cortical Off-R. Functional connectivity analysis showed that ACX areas varied in their intrinsic network structure. Imaging of medial geniculate body (MGB) axons showed a thalamic origin of the parallel On and Off-R circuits and that spatial convergence and co-activation of MGB inputs determine cellular On and Off preference. Altogether, our results demonstrate that ACX fields differentially process sound onset/offset via parallel and spatially patterned projections from the MGB and are refined by specific intracortical connectivity.

RESULTS

We set out to investigate the spatial organization of temporal sensitivity in mouse ACX on multiple spatial scales. Because ACX responses, especially Off-Rs, are temporally sensitive to anesthesia (Fishman and Steinschneider, 2009; Joachimsthaler et al., 2014; Qin et al., 2007; Recanzone, 2000), we performed our studies in ACX of awake animals. We used F1s of CBA/CaJ and Thy1-GCaMP6s (C57BL/6 background) crosses (Dana et al., 2014), which show normal adult hearing (Frisina et al., 2011) and widespread cortical expression of GCaMP6s.

We first investigated the spatial distribution of On-Rs and Off-Rs on the mesoscale using WF imaging. We imaged the left ACX of awake adult mice (n = 13) while presenting 2 s pure tones (Figure 1A). Tone onset resulted in spatially restricted fluorescence increases at several locations in ACX (Figure 1B, see 0.4 s following tone On; Figure S1A). Fluorescence increases were widespread in ACX, with the largest increases present in discrete locations corresponding to activations of primary, as well as higher-order, ACX areas, putatively A1, the anterior auditory field (AAF), and secondary ACX (A2), respectively. Following tone offset, we observed additional widespread increases of fluorescence (at 2.4 s, or 0.4 s after tone offset), which corresponded to an Off-R (Figure 1B). Off-Rs are not due to changes in animal state after tone cessation (Figure S2). On-R and Off-R were also present in response to ultrasonic frequencies such as 83.0 kHz (Figure 1B). In both examples, the spatial pattern of On-R qualitatively matches previous results (Baba et al., 2016; Issa et al., 2014; Tsukano et al., 2015).

Varying sound frequency and level showed that both On-R and Off-R changed their response locations with respect to tone frequency (Figure S1). We overlaid contours of the strongest activations across ACX for each frequency at the respective thresholds of On-R (Figure 1C) and Off-R (Figure 1D). Clear systematic changes of activated areas can be seen in multiple locations. Based on the relative positions of these gradients in On-R, we labeled areas as A1, AAF, and A2. The gradients were consistent across animals (Figure S3). A1 shows dual tonotopic axes: one from the caudal area toward the dorsomedial area (ultrasonic field [UF]) and the other one reaching toward the ventrolateral side (Figure 1C), largely consistent with prior reports (Issa et al., 2014; Polley et al., 2007; Tsukano et al., 2015) but with the subtle difference that two On-tonotopic gradients in A1 share the low- to mid-frequency axis before splitting dorsally and ventrally. In addition, we observed that a tonotopic gradient is present for Off-Rs in A1, AAF, and A2 in all animals (Figure 1D; Figure S3B). The Off-tonotopic gradient from A1 to UF overlapped with the On-tonotopic gradient. However, the Off-tonotopic gradient also extends dorsoposteriorly and thus covers more area dorsally than the On-tonotopic gradient. Between these dominant gradients of strong tone responses there was a weakly responding central region, consistent with previous WF studies (Issa et al., 2017). Thus, Off-Rs are present in multiple ACX areas and Off-Rs are tonotopically organized. The differences in the tonotopic gradients between On-Rs and Off-Rs suggest that different microcircuits might underlie On and Off processing.

Distinct ACX Areas Show Selectivity to Temporal Features

So far, we identified functional ACX areas based on separate On and Off-Rs at threshold. Because these areas showed overlap, we sought to determine whether ACX contained distinct functional areas based on the combination of selectivity for On and Off-R throughout frequency and sound-level combinations and whether such ACX segmentations could identify unique ACX areas. We developed an unsupervised and unbiased image segmentation technique that takes the entire temporal response of each pixel into account. We expressed the temporal activities of pixels as a linear combination of spatially distinct regions of interest (ROIs) weighted by temporal modulations (Figure 2A) using an autoencoder with non-negativity constraints on the spatial weights (Whiteway and Butts, 2017). An autoencoder is a neural network with one or more hidden layers (Figure 2B). While the input and output layers have the same number of nodes, the autoencoder reduces the dimension in the image sequence by expressing the intensity of each pixel as the weighted sum of the activity of the hidden layer, which has a smaller dimensionality. These weights are interpreted as distinct spatial patterns of activity (or ROIs), and the activity of the hidden layer reflects the temporal modulation (Figure 2C).

Typically, an autoencoder with ~50 ROIs well approximated the acquired image sequence (Figure S4A). The resulting ROIs densely tiled the imaged area (Figures S4B and S4D) with minimal spatial overlap (Figure S4C), which reflects the distinct selectivity of On and Off-Rs of different ACX fields while making parsing ACX fields unambiguous. In addition, the minimal overlap is likely due to our choice of the minimum number of ROIs to the desired degree of goodness of fit (Figure S4A). Adding ROIs increases overlap but does not increase goodness of fit (Figure S4A). To verify our method, we compared the locations of the ROIs with evoked fluorescence increases. We found that ROI placements agreed with locations of activation for both On-R (Figures 2D and 2E) and Off-R (Figures 2F and 2G), and their shapes reflected the contours of fluorescence increases. Thus, our method reliably identifies regions of common activations and extracts their temporal activations without prior knowledge of the spatial distribution of activity. This approach provides advantages over the common square/hexagonal grid segmentation, because the choice of grid size could be arbitrary and might obscure the temporal selectivity of ROIs by grouping functionally separate fields together. Here, we segmented ACX

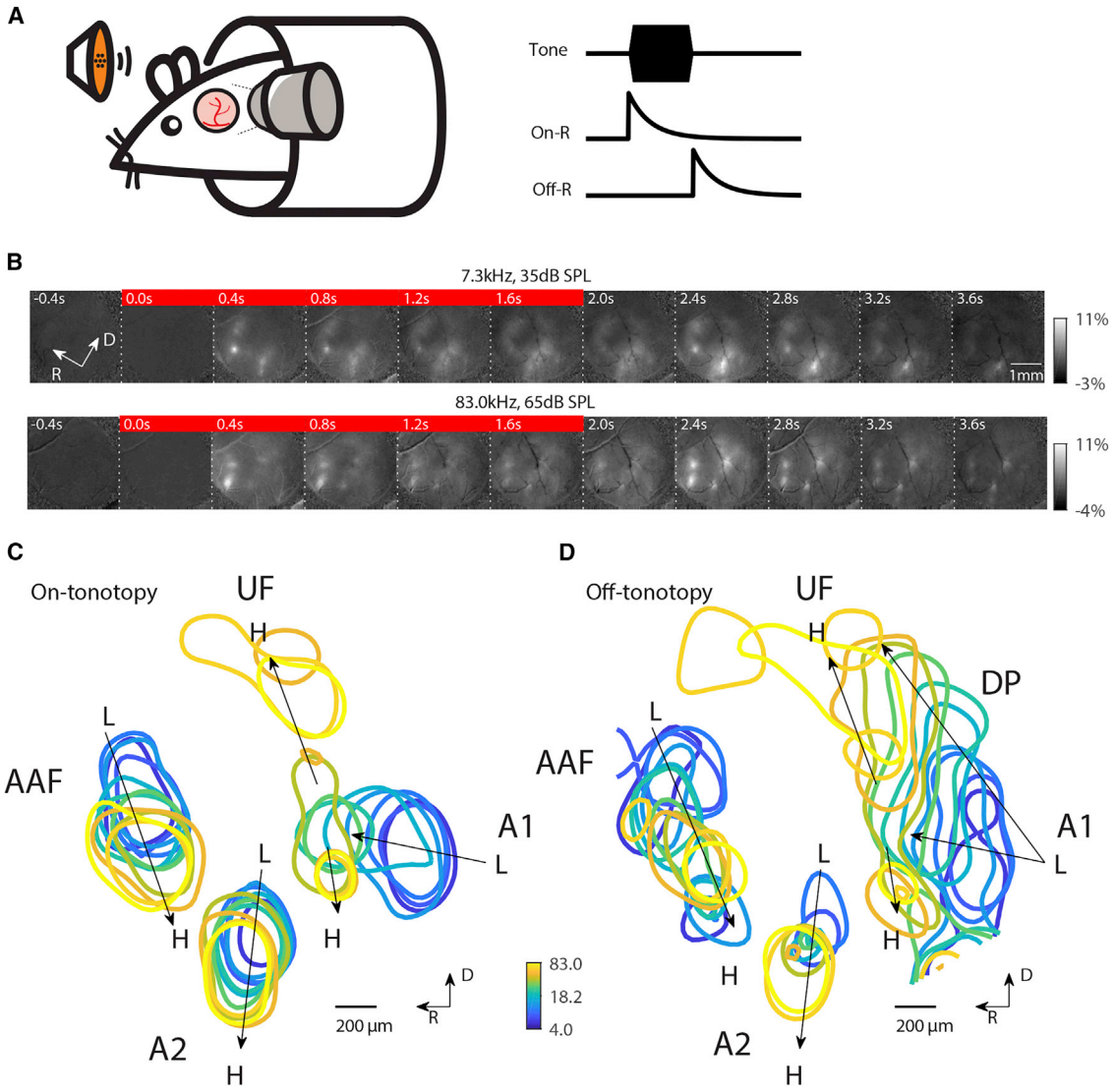

Figure 1. Both On-R and Off-R Show Global Tonotopy

(A) Experimental paradigm: head-fixed mouse passively listened to tones while ACX was imaged. On-Rs and Off-Rs are defined as increases in fluorescence following tone onset and offset, respectively.

(B) Sequence of WF images showing responses to a 7.3 kHz tone at 35 dB SPL and a 83.0 kHz tone at 65 dB SPL. The red bar indicates the images collected during tone presentation (0–2 s).

(C) On tonotopy showing the contour of the 95th percentile of the responses following tone onset. A systematic shift of maximum activation location can be seen in A1, AAF, and A2.

(D) Same as in (C) but for Off tonotopy. The center of ACX shows weaker tone-evoked responses and thus is not marked by contours.

into functional fields, but our method can be applied to arbitrary WF datasets for spatiotemporal analysis and image segmentation.

Identified ACX fields show distinct On and Off-frequency response areas (FRAs) (Figures 2H and 2I), indicating that differences in the sensitivity to temporal features are a major determinant of ACX organization. The low-frequency selective A1 ROI (Figure 2I, A1(L)) shows predominant On and Off-R for tones of 4.0 to 7.3 kHz, while the mid-frequency selective A1 ROI (Figure 2I, A1(M)) responded mostly to frequencies around 18.2 kHz. The high-frequency selective A1 ROI (ventrolateral gradient of A1) (Figure 2I, A1(H)) typically has On and Off-Rs similar to those of mid-frequency A1 due to spatial proximity and the diffuse nature of WF signals. However, the average On-R of high-frequency A1 ROI to 61.3 kHz is larger than that of mid-frequency A1 ROI at threshold. In contrast, UF ROI shows much higher selectivity to high frequencies (Figure 2I, UF), consistent with the proposed role in processing conspecific ultrasonic vocalizations (Stiebler et al., 1997). Dorsoposterior (DP) ROI shows stronger Off-R (Figure 2I, DP). AAF ROI (Figure 2I, AAF) shows comparable On and Off-R, while A2 ROI (Figure 2I, A2) shows weaker Off-R. Lastly, the center region

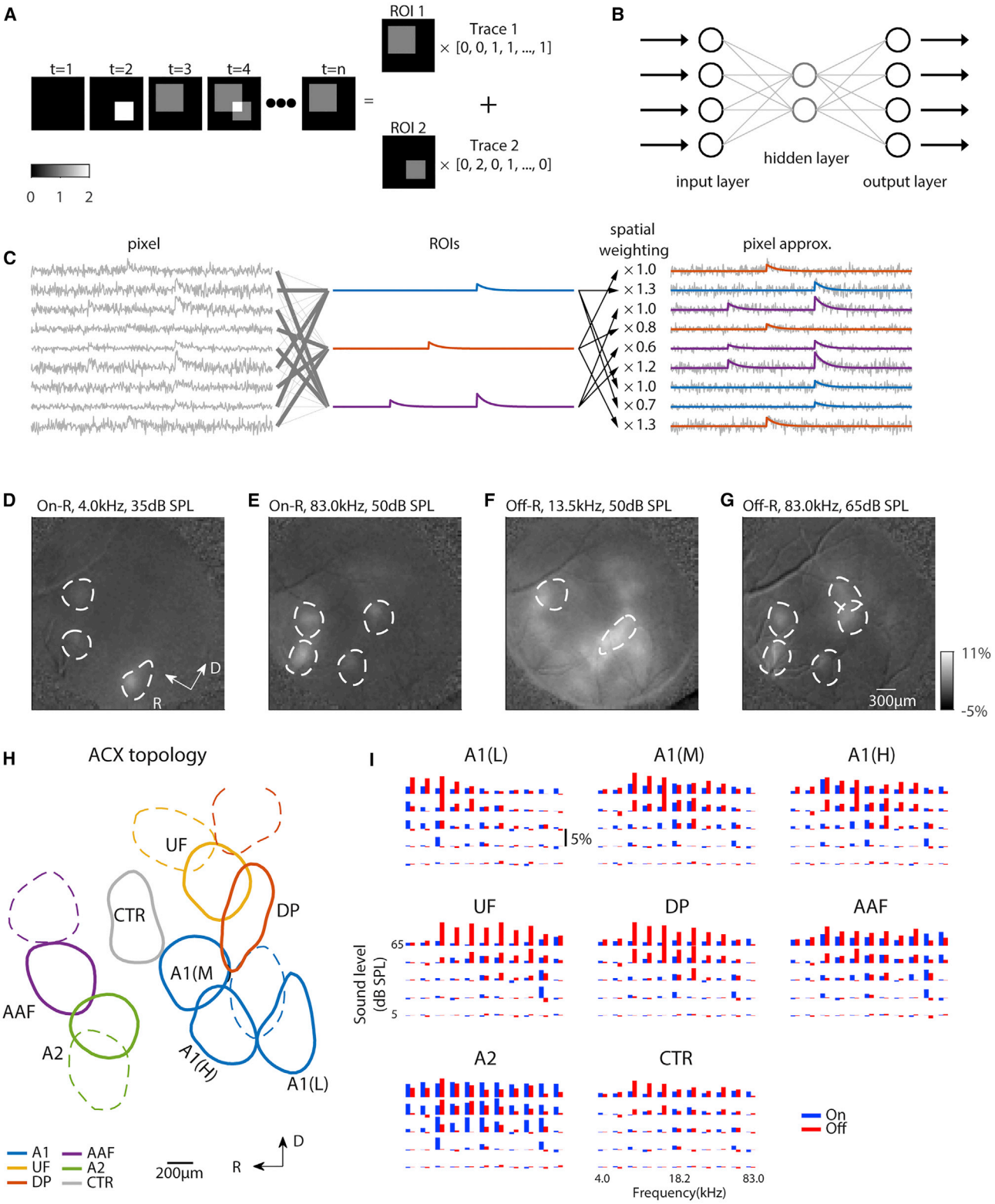

Figure 2. WF Image Segmentation Using an Autoencoder Reveals ACX Areas with Distinct On and Off Selectivity

(A) Cartoon showing image segmentation. The example image sequence at any time point can be expressed as the weighted summation of ROI 1 and ROI 2 by respective activity level. Our goal of image segmentation is to retrieve activated areas, as well as their temporal activation traces.

(legend continued on next page)

(Figure 2I, CTR) shows weaker responses and is likely less sensitive to simple stimuli such as pure tones (Figure 2H; Figure S4F). The spatial layout of these ROIs was consistent across mice (Figure S3). Thus, ACX contains functional areas with distinct sensitivity to temporal features. Our image segmentation approach can better subdivide ACX, because it captures the different temporal dynamics of ACX fields.

ACX Fields Differ in Thresholds and Sound-Level Dependence of On-Rs and Off-Rs

We next characterized threshold and sound-level dependence of parsed ACX fields. Off-Rs in all areas showed a higher threshold than On-Rs, and Off-Rs can have higher amplitudes than On-Rs (e.g., at 50 and 65 dB sound pressure level [SPL]) (Figures 3A–3E). UF and DP showed the highest Off-R preference at 65 dB SPL (Figure 3F). Thus, while core ACX fields (e.g., A1 and AAF) robustly respond to both tone onset and offset, areas away from core fields can show dominant Off-Rs, especially for loud tones.

Off-Responsive Areas Are More Spatially Extensive than On-Responsive Areas

The different selectivity for On and Off-R in ACX fields suggest a different underlying circuit topology. To quantify the large-scale spatial topology, we computed signal correlations (SCs) between individual ROIs among a dorsal-ventral slice in each ACX area. In A1 and UF, Off-SCs were significantly higher than On-SCs (Figures 3G and 3H). This relationship was maintained over distance, suggesting that Off-Rs are more spatially extensive in the dorsal direction (Figures 3G and 3H). This pattern was also true across ACX (Figure 3I), suggesting that Off-Rs are more diffusively represented in all ACX areas. These results are consistent with dorsal ACX areas, especially UF and DP, having dominant Off-R (Figure 3F). Altogether, the areal differences in the tonotopic gradients (Figure 1) and the differences in SCs between On and Off-Rs suggest that different intrinsic and ascending microcircuits within each area underlie the regional differences in On and Off processing.

Neural Populations in ACX Areas Differ in Their Selectivity to Sound Onset or Offset

To investigate areal differences in processing tone onset and offset, we sought to analyze local microcircuits and assessed the temporal stimulus preferences of single neurons in four ACX areas using *in vivo* two-photon imaging. (n = 32 mice; A1: 67 fields of view (FOVs), 19,366 cells; AAF: 24 FOVs, 5,425 cells; A2: 20 FOVs, 5,918 cells; DP: 8 FOVs, 2,573 cells). Cells in all ACX areas could show time-locked responses to tone onset and/or offset (Figures 4A and 4B; Figure S5). Cells showing On-R were sparse (A1, 5.05% ± 2.89%; AAF, 5.36% ± 2.58%; A2, 5.83% ± 4.53%; DP, 2.23% ± 1.29%, among all neurons imaged), and the same was true of Off-R (A1, 6.62% ± 4.34%; AAF, 2.14% ± 1.83%; A2, 2.28% ± 2.24%; DP, 4.64% ± 2.42%, among all neurons imaged), consistent with a sparse representation of sound in ACX in electrophysiological studies (Hromádka et al., 2008). Few neurons showed both On-Rs and Off-Rs (A1, 0.98% ± 0.90%; AAF, 0.54% ± 0.54%; A2, 0.95% ± 1.31%; DP, 0.43% ± 0.57%, among all neurons imaged) (Figure S6A), suggesting that most layer (L) 2/3 neurons are either only On responsive or Off responsive. We quantified the selectivity of On and Off-Rs by computing the On and Off-R bias index (OBI = (Off-R − On-R)/(Off-R + On-R)) (Figure 4C). Most OBI values were −1 (On-only) or 1 (Off-only). In A1 and DP, Off-only neurons (53% and 65% of neurons) outnumber On-only neurons (38% and 28% of neurons), while in A2 and AAF, the reverse is true (67% and 70% versus 23% and 19% of neurons). Neurons showing both On-R and Off-R constituted ~10% of responding neurons and were more Off biased in A1 and DP than in AAF and A2 (Figure 4D). We confirmed these results in a separate analysis (Figure S6). Altogether, these results show that ACX areas differ in both number of On and Off-only cells, as well as in On and Off selectivity of individual cells. Thus, ACX areas are defined by the underlying population representation of tone onset and offset and cellular response amplitudes.

To confirm our results and to sample across layers, we implanted 16-channel linear multielectrode arrays into A1, spanning a cortical depth of 800 μm. We first analyzed the local field potential (LFP), which reflects the combination of local neuronal activity and afferent input into A1 (Herreras, 2016; Katzner et al., 2009; Liu et al., 2015). We found that more tone frequencies evoked Off-R compared to On-R (Figures S7A–S7C), consistent with the widespread nature of Off-R (Figure 3). Moreover, distribution of OBI of all electrode contacts shifted toward Off-R (Figure S7D). These results confirm that Off-R evokes wide activation in A1 and that A1 responses are biased toward Off-R.

Prior electrophysiology studies reported a higher proportion of neurons showing both On-R and Off-R than our imaging results (Joachimsthaler et al., 2014; Qin et al., 2007; Tian et al., 2013). To identify potential sources for this discrepancy, we recorded single units (n = 220) from A1 of awake mice and analyzed their On and Off-R (Figures S7F–S7H). 200/220 units (91%) were responsive to either tone onset or offset. Among these units, 26% had only On-R, 57% had both On-R and Off-R, and 7% had only Off-R. We classified neurons based on their spike shape (wide versus narrow), reflecting putative excitatory and inhibitory units and analyzed their OBI. Both classes showed similar OBI distributions (Figure S7G). Analyzing OBI across depth showed that

(B) Autoencoder is a neural network with one or more hidden layers between input and output layers, which have the same number of nodes. The weights between input or output layer and hidden layer are adjusted such that the output matches the input as closely as possible. The hidden layer typically has fewer nodes than the input or output layer to achieve dimension reduction.

(C) Principle of fitting autoencoder ROIs. Original pixels (left) are linearly combined to produce ROIs (middle) such that each pixel can be approximated (right) in turn by the linear combination of these ROIs, while the weights are interpreted as the spatial profile of the ROIs.

(D–G) On-R and Off-R spatial profiles overlaid with selected autoencoder ROIs to validate ROI placement. (D)–(G) share a color scale. (D) On-R to 4.0 kHz at 35 dB SPL. (E) On-R to 83.0 kHz at 50 dB SPL. (F) Off-R to 13.5 kHz at 50 dB SPL. (G) Off-R to 83.0 kHz at 65 dB SPL.

(H) Parcellation of ROIs into ACX fields. ROIs outlined in solid lines have the On and Off-frequency response areas (FRAs) shown in (I).

(I) On and Off-R amplitude is plotted as a function of frequency and sound level for ACX fields. Adjacent blue and red bars represent On and Off-R to the same frequency and sound-level combination.

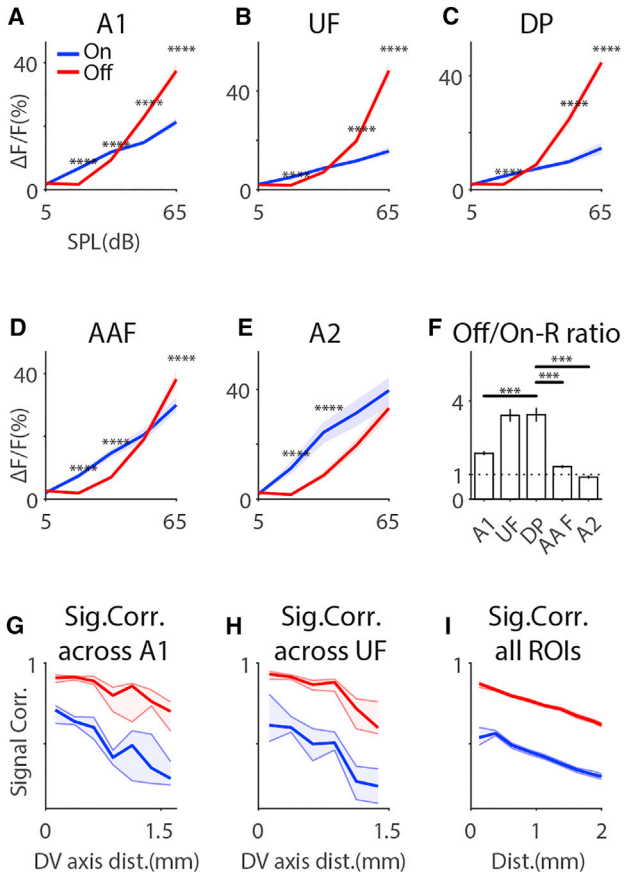

Figure 3. On and Off-R Show Areal Differences in Amplitude and Spatial Distribution

(A–E) Differential On-R and Off-R profile as a function of both sound level and ACX field ((A) A1; (B) UF; (C) DP; (D) AAF; (E) A2). On-R and Off-R profiles with respect to sound level for different ACX fields were obtained by summing over frequency in On and Off-FRAs. ***$p < 0.001$; ****$p < 0.0001$. Shaded regions show the 95% confidence interval.

(F) Off-R and On-R ratio at 65 dB SPL as a function of ACX fields. Error bars show SEM.

(G) On and Off-SC as a function of distance along the dorsal-ventral axis, calculated among ROIs dorsal to A1 ROIs. Off-Rs show higher SCs than On-Rs. Shaded regions show the 95% confidence interval.

(H) On and Off-SC calculated among ROIs dorsal to UF ROIs. Shaded regions show the 95% confidence interval.

(I) On and Off-SC among all ROIs. Shaded regions show the 95% confidence interval.

OBI was depth dependent, with deeper-layer units more biased to On-R (Figure S7H). Altogether, these results suggest that A1 contains both On and Off-only neurons and that there is a depth-dependent distribution of these neurons consistent with sublaminar circuit differences in L2/3 (Meng et al., 2017).

Local Tonotopy Is Heterogeneous for Both On-R and Off-R in All Areas

Both On-R and Off-R show large-scale tonotopy (Figures 1 and 2), whereas cellular frequency selectivity is heterogeneous in anesthetized A1 (Bandyopadhyay et al., 2010; Kanold et al., 2014; Rothschild et al., 2010). We tested whether Off-R exhibited local tonotopy and whether On-R and Off-R cells differed in local heterogeneity of frequency preference. We compared the degree to which On-R and Off-R are locally tonotopically organized by analyzing separate linear models between best frequency and spatial locations of cells (Figure 4E). We found low local tonotopy of frequency selectivity, because the goodness of fit (R^2) was low, consistent with prior studies (Bandyopadhyay et al., 2010; Maor et al., 2016; Rothschild et al., 2010). Moreover, the models showed a similar R^2 for On-R or Off-R across ACX areas, suggesting that the local heterogeneity of frequency selectivity between On-R and Off-R is similar within and across mouse ACX fields.

ACX Areas Differ in the Spatial Pattern of Neuronal Correlated On-R and Off-R Activity

Our results indicate regional differences in cellular selectivity. To gain insight into the spatial distribution of ACX circuits, we calculated pairwise SCs, which are reflective of shared inputs (Shadlen and Newsome, 1998). In A1, On-SCs are highest for nearby neurons and decrease with distance, consistent with results in anesthetized mice (Figure 4F) (Winkowski and Kanold, 2013). Such a decrease is also present in A2, while DP shows a patchy distribution of On-SCs and AAF shows a weak SC gradient. Off-SCs were larger than On-SCs in most areas except for DP. In A1, these differences between On-SC and Off-SC were widespread, while such differences were present in patchy areas in AAF (~150–175 μm) and A2 (~50–275 μm). We validated this result by computing the SC among chronically implanted linear electrode contacts; a similar correlation structure was seen, in which Off-SC was higher than On-SC over distance (Figure S7E). These results show that Off-R neurons are more widespread among different cortical columns and along cortical depth, which could be due to a difference in the underlying intrinsic circuits or due to the spatial distribution of the ascending input.

Granger Causality Analysis Reveals Areal Differences in Functional On and Off Networks

The areal differences in SCs suggest different underlying neuronal networks. We sought to identify the functional networks in the different ACX areas by performing Granger causality (GC) analysis separately among On-R and Off-R neurons (Francis et al., 2018; Friston et al., 2013; Granger, 1969; Oya et al., 2007; Sheikhattar and Babadi, 2016; Sheikhattar et al., 2018). GC analysis provides a data-driven framework for inferring causal interactions between neurons by statistically testing whether a neuron's activity can be predicted by the recent activity history of other neurons and thus uncovering functional networks (Francis et al., 2018; Granger, 1969; Sheikhattar and Babadi, 2016). The causal interactions (GC links) can take positive or negative signs, reflecting correlated or anticorrelated neuronal activities, respectively (Francis et al., 2018). Our calcium indicator is expressed in excitatory neurons; thus, we focused on positive GC links. An example of two GC-linked neurons is shown in Figure 5A. The source trace preceded the target trace. Figure 5B shows one example FOV, with the most significant GC links labeled. We quantified the number, strength, length, and directionality of the GC links. In A1 and DP, Off-GC links outnumbered On-GC links, while the opposite was true in

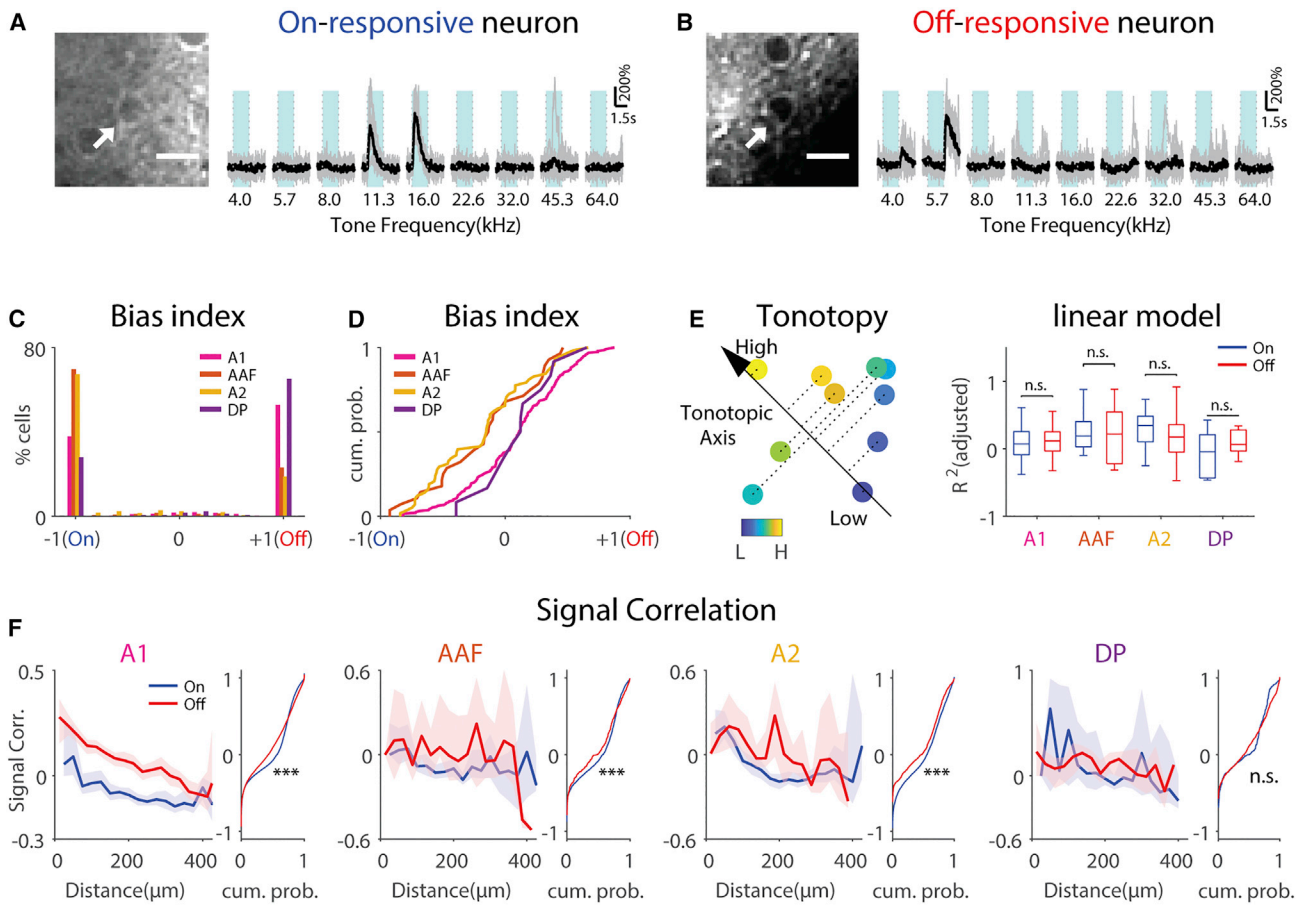

Figure 4. L2/3 Neurons Show Distinct On-R and Off-R and Are Differentially Distributed across ACX Areas

(A) Example On-R neuron (arrow). Vertical dotted lines indicate tone onset and offset, respectively. Light blue areas indicate tone duration.

(B) Example Off-R neuron. Scale bar: 10 μm.

(C and D) Histogram of cellular OBI values as a function of ACX fields (C). OBI = (Off-R − On-R)/(Off-R + On-R), while (D) shows the cumulative distribution function (CDF) of values other than −1 and 1. Wilcoxon rank-sum test; A1 versus AAF: z = 2.77, p = 0.0056; A1 versus A2: z = 4.41, p = 1.02×10^{-5}; DP versus AAF: z = 1.93, p = 0.053; DP versus A2: z = 2.49, p = 0.013.

(E) Left: cartoon showing a linear model to predict the best frequency (BF) of On-R and Off-R with respect to the cell's spatial locations. A direction is searched onto which the projection of the cell's coordinates best explains the cell's BF. Right: goodness of fit of On-R and Off-R in cells of different ACX fields.

(F) Relationship between On- and Off-SCs and pairwise distance on the neuronal level. Solid lines show the median, while shading indicates the 95% confidence interval. The flanking panel shows CDF of On-SC and Off-SC not regarding distance. ***p < 0.001. **p < 0.01. Rank-sum test; A1: z = −13.6, p = 4.33×10^{-42}; AAF: z = −3.52, p = 4.30×10^{-4}; A2: z = −8.73, p = 2.07×10^{-18}; DP: z = −2.93, p = 3.4×10^{-3}.

AAF and A2 (Figure 5C). These differences indicate higher respective interconnectivity and are consistent with the differences in the relative numbers of On-R and Off-R neurons. In contrast, GC link strength (J statistics) largely showed no difference except for AAF (Figure 5D), suggesting both On and Off networks are strongly functionally connected. Because most cells had either On-R or Off-R, these results indicate that ACX areas contain separate interdigitated On and Off networks.

We next extracted the spatial properties of GC links for On and Off networks. First, Off-GC links tend to have more short links in A1 (Figure 5E), suggesting that Off-GC networks more densely cover the neural populations in A1 and are more spatially clustered. Other ACX fields showed no length differences (Figure 5E). Because ACX areas have large-scale tonotopic maps, we next investigated whether GC links also show a direction preference. Except for DP and A2 Off-Rs, the distributions of the GC-link directions significantly deviate from uniform distributions (Figure 5F). In A1, AAF, and A2, the ellipse-like distributions have the long axis, reflecting a spatial bias of cell pair interactions, roughly in parallel to the tonotopic axes. Thus, although local cellular populations lack precise tonotopic, there are regularities in their functional connectivity whose spatial patterns are closely related to the tonotopic axis. Moreover, we found no difference in the On-/Off-GC-link direction distribution (Figure 5F). Lastly, the distribution of GC-link directions in AAF appeared to be narrower than in A1 or A2. We thus combined both On and Off-GC links and compared the spread in the direction of the short axis of the eclipse-like distributions. AAF GC links were more narrowly distributed than those in A1 (p = 0.033) and the difference between AAF and A2 was close to significance (p = 0.058). Thus,

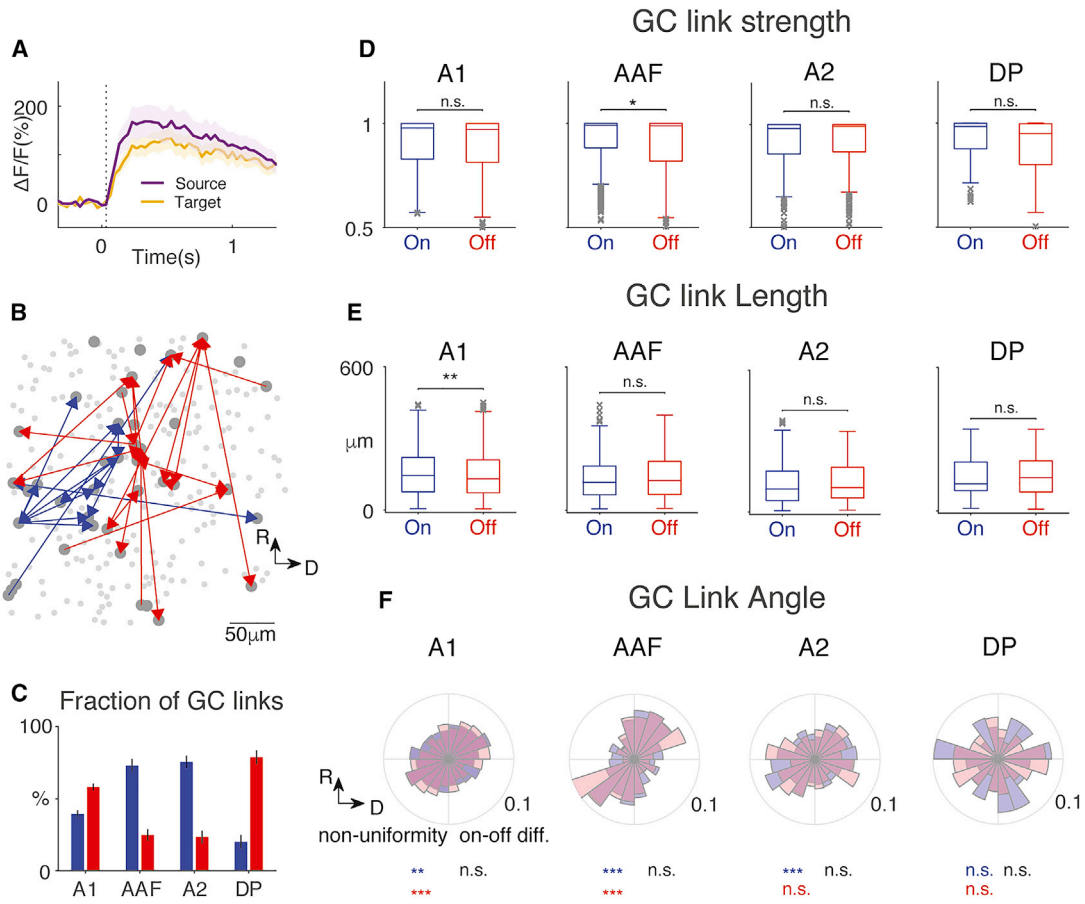

Figure 5. GC Analysis Reveals Distinct On and Off Subnetworks

(A) Fluorescence time course of GC-linked cells.

(B) Example field: On (blue) and Off (red) GC links. Only GC links with J statistics > 0.95 are shown for clarity.

(C) Proportion of GC links (false discovery rate: 0.001). More Off-GC links in A1 and DP. Wilcoxon rank-sum test; On versus Off: A1, $p = 2.53 \times 10^{-7}$, $z = -5.16$; DP, $p = 1.55 \times 10^{-4}$. More On-GC links in AAF and A2. AAF: $p = 5.44 \times 10^{-7}$, $z = 4.55$; A2: $p = 3.32 \times 10^{-6}$, $z = 4.65$.

(D) J statistics, a measure of GC-link strength. Only AAF shows a slightly higher On-GC-link strength. Wilcoxon rank-sum test, $p = 0.0175$, $z = 2.38$.

(E) GC-link length. A1 contains shorter Off-GC links. Wilcoxon rank-sum test, $p = 0.0022$, $z = 3.06$.

(F) Distribution of the direction of GC links. The nonuniformity of the distributions was tested using the chi-square goodness-of-fit test. A1: On, $p = 0.043$, Off, $p = 1.08 \times 10^{-22}$; AAF: On, $p = 1.48 \times 10^{-7}$, Off, $p = 7.77 \times 10^{-4}$; A2: On, 8.15×10^{-4}, Off, $p = 0.42$; DP: On, $p = 0.89$, Off, $p = 0.17$. On and Off distribution difference: two-sample Kolmogorov-Smirnov test; A1: $p = 0.065$; AAF: $p = 0.82$; A2: $p = 0.68$; DP: $p = 0.85$.

the spatial topology of the intrinsic functional architecture of L2/3 in different ACX fields differs. Altogether, these results indicate that although On and Off-R populations are largely nonoverlapping, they are spatially intermingled and parallel, consistent with the salt-and-pepper structure in L2/3 of mouse ACX (Bandyopadhyay et al., 2010; Rothschild et al., 2010).

The On and Off Responsivity of MGB Terminals Determines Areal Responses

So far, our results indicate that ACX contains distinct functional areas defined by differing cellular selectivity and intrinsic connectivity. Because ascending inputs to ACX neurons determine the initial cellular selectivity to sound dynamics, we examined how the cellular On and Off selectivity emerged from ACX inputs. The main ascending inputs to ACX are provided by MGB axons, which terminate on excitatory neurons ranging from L2/3 to L6, with the strongest input in L4 (Ji et al., 2016). Because different ACX areas receive dominant input from different subdivisions of the MGB, we speculate that these sets of synapses reflect separate pathways from the MGB. To test this hypothesis, we injected the adeno-associated virus (AAV)-expressing GCaMP6s into the MGB (n = 7 mice) and imaged axon terminals in A1 (20 FOVs) (Figure S8). We focused on A1 because of its distinct difference in On and Off-Rs and because prior *in vivo* patch-clamp recordings showed that in A1, On-Rs and Off-Rs are driven by nonoverlapping sets of synapses (Scholl et al., 2010). MGB terminals showed prominent On-R or Off-R (Figures 6A and 6B). Few MGB terminals showed both On-R and Off-R (0.88% ± 1.06%). The proportion of MGB terminals showing either On-R or Off-R was similar (Figure 6C), and most terminals were either On only or Off only (Figure 6D). Thus, most MGB terminals either relay On-R or Off-R, suggesting the existence of distinct parallel

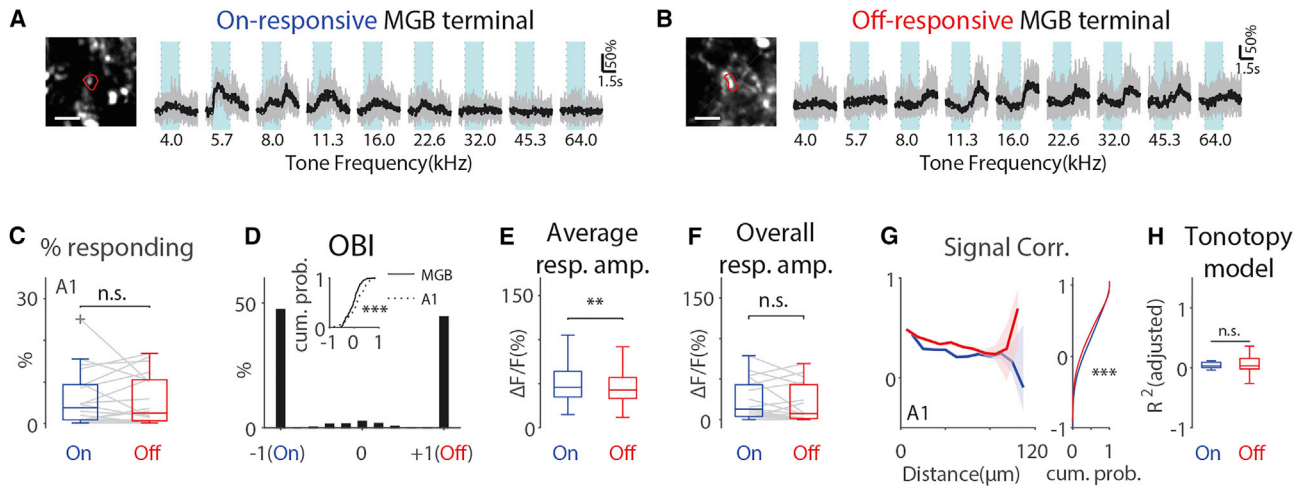

Figure 6. MGB Terminals in A1 Largely Show Either On-R or Off-R, and Off-R Terminals Show Higher Local Signal Correlations

(A) On-R terminal. The image shows the contour of the terminal in red. Scale bar: 5 μm. Light blue areas indicate tone duration.

(B) Same as in (A) but showing an Off-R terminal.

(C) Proportion of On-R or Off-R terminals is similar. On, 5.99% ± 6.72%; Off, 5.62% ± 6.00%; paired t test, t(20) = 0.34, p = 0.74.

(D) Histogram of OBI values of MGB terminals in A1. Inset shows CDFs of OBI values other than −1 and 1 from MGB terminals and A1 L2/3 neurons. Wilcoxon rank-sum test, z = 3.64, p = 2.71 × 10^{-4}.

(E) Individual MGB terminals in A1 show significant larger On-Rs. Wilcoxon rank-sum test, z = 2.91, p = 0.0036.

(F) Overall On and Off-R amplitude (see STAR Methods). Wilcoxon rank-sum test, z = 0.85, p = 0.39.

(G) Off-Rs show higher Off-SCs over distance (0–70 μm). Shaded regions show the 95% confidence interval around the median. Right: cumulative distribution function of all On- and Off-SCs. ***p < 0.001.

(H) Goodness of fit of the linear On-R and Off-R tonotopy model in MGB terminals in A1 was similar.

MGB to A1 pathways. Terminals showing both On-R and Off-R had a more negative OBI compared to the distribution of OBI of the cellular response (Figure 6D, inset), suggesting that a transformation of On-R and Off-R selectivity exists from MGB terminals to A1 cellular responses, which are more Off-R biased. Moreover, given the prevalence of Off-R A1 neurons, this suggests a differential amplification of Off-Rs from MGB inputs to yield a larger fraction of Off-R neurons.

To gain insight into the transformation, we compared the average strength of On and Off-R pooled across terminals. Terminal On-Rs were larger than Off-Rs (Figure 6E), which is similar to the cellular responses (Figure S6B). However, unlike the cellular response in A1, the On-R and Off-R MGB terminals have similar overall response amplitudes (Figure 6F). This suggests that the Off-R dominance in A1 cells was not generated by stronger or more numerous Off-R MGB afferents.

Convergence and temporal synchrony of thalamic inputs can strongly influence cortical neurons (Bruno and Sakmann, 2006), which could lead to stronger cellular responses. We observed a distinct spatial SC structure in mesoscale (Figures 3G–3I), as well as in cellular responses (Figure 4F). These properties could result from spatially structured MGB input, and we found that MGB terminals had higher Off-SCs (Figure 6G) consistent with the cellular data. We also investigated the distance dependence of On and Off-SC of MGB terminals and found that Off-SC was higher than On-SC over a distance of 0–70 μm, indicating a larger spatial spread of terminal Off-R. These results suggest that although individual MGB terminals do not respond to tone offset more strongly than to tone onset, the spatial correlation structure of MGB inputs is transformed into cellular tuning in A1 and leads to a more spatially extensive representation of tone offset.

Lastly, we investigated whether there are tonotopic structures in MGB terminal responses. A linear model did not reveal a tonotopic structure in either On-R or Off-R in MGB terminals (Figure 6H), consistent with reports that local On-R MGB projections to A1 show spatially heterogeneous tuning (Vasquez-Lopez et al., 2017). Altogether, our results suggest that the spatial mesoscale distribution of On and Off-R A1 neurons is largely inherited from the spatial distribution of On and Off-R MGB terminals.

Cortical Inhibitory Networks Can Amplify Off-R through Disinhibition

The activity of cortical neurons is influenced by inhibition, and we hypothesized that the On and Off selectivity of ACX L2/3 excitatory neurons is actively shaped by the local inhibitory network. To investigate this question, we focused on PV- and SOM-positive interneurons, which are thought to control the activity of L2/3 neurons via a disinhibitory circuit (Pfeffer et al., 2013). We crossed Thy1-GCaMP6s mice with either PV-cre or SOM-cre mice and injected AAV-expressing mRuby and GCaMP6s under control of the flip-excision (FLEX) switch sequence into ACX of F1 animals. Thus, PV or SOM interneurons could be identified based on the nuclear red fluorescence signal while allowing simultaneous imaging of Thy1+ excitatory neurons and PV or SOM neural populations (Figures 7A and 7C) (Thy1xPV-cre: 8 mice, 427 PV neurons; Thy1xSOM: 6 mice, 288 SOM neurons). We presented 2 s tones and found that although some PV and

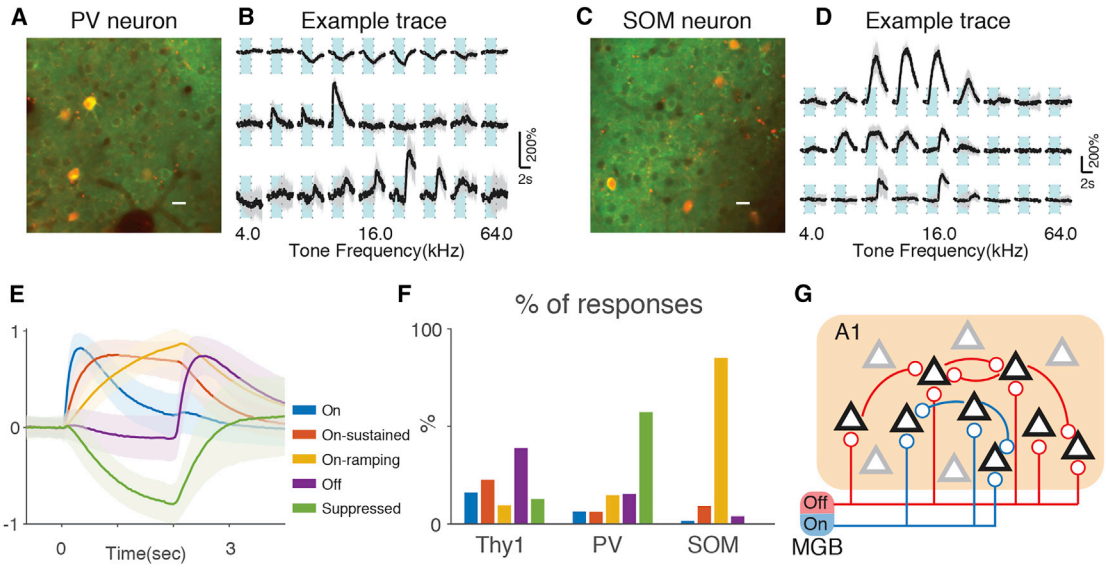

Figure 7. PV and SOM Neurons Show Distinct Temporal Dynamics in Response to Prolonged Tones

(A) Example FOV showing both Thy1-GCaMP6s cells and PV-positive interneurons expressing GCaMP6s and mRuby. Scale bar: 10 μm. Light blue areas indicate tone duration.

(B) Example PV interneurons showing suppressed response (top), On-R (middle), and Off-R (bottom).

(C) Example FOV showing both Thy1-GCaMP6s cells and SOM-positive interneurons expressing GCaMP6s and mRuby.

(D) Example SOM interneurons showing slow ramping responses following tone On (top and middle) and Off-R (bottom).

(E) k-means clustering on responses by Thy1, PV, and SOM cells. All traces were normalized to maximum absolute amplitude before they were averaged within each cluster. Shaded regions show SD.

(F) Thy1, PV, and SOM cells show distinct proportion of response types.

(G) We propose that cortical On and Off-R result from largely segregated On and Off thalamic input and that the spatial patterns of these inputs determine the spatial layout of On and Off-R selective neurons. Furthermore, Off-R cortical neurons have more recurrent connections that amplify the thalamic input compared to On-R circuitry. Black triangles represent On and Off-R neurons, and gray triangles represent unresponsive neurons.

SOM interneurons displayed typical On and Off-R similar to those seen in excitatory neurons, most interneurons displayed slower temporal dynamics (Figures 7A and 7B). Most PV neurons showed a slow decrease in fluorescence following tone onset (Figure 7B). Although a subset of suppression responses showed a brief positive deflection immediately after tone onset, their occurrence was rarer than pure suppression responses (Figure S9). SOM neurons showed similarly slow temporal responses, albeit positive in sign (Figure 7D). To classify different response types, we performed k-means clustering on significant responses averaged across trials, pooling responses from both Thy1 and PV or SOM cells. We could identify 5 clusters with distinct temporal dynamics. Cluster 1 shows a sharp increase in fluorescence following tone onset and decays afterward (Figure 7E, On). Cluster 2 shows a more graded fluorescence increase, which sustains during tone presentation (Figure 7E, On-sustained). Cluster 3 shows even slower rise with little plateau and decays following tone offset (Figure 7E, On-ramping). Cluster 4 shows a sharp increase after tone offset and is categorized as typical Off-Rs (Figure 7E, Off). Cluster 5 has dynamics similar to those of On-ramping while opposite in sign (Figure 7E, Suppressed). The proportion of responses assigned to each cluster differed among cell types (Figure 7F). Thy1 responses are mostly Off, On, and On-sustained. PV interneurons mostly show Suppressed responses, while SOM interneurons show mostly On-ramping responses. These two response clusters show no difference in latency reaching half-peak amplitude (0.95 ± 0.36 s versus 0.85 ± 0.26 s, $p = 0.21$, Wilcoxon rank-sum test). The opposite responses suggest that SOM neurons suppress PV neurons during prolonged tone activation, consistent with a disinhibition circuit scheme (Pfeffer et al., 2013). The inhibitory postsynaptic current from SOM to PV interneurons could last until after tone offset, despite the cessation of firing of SOM interneurons. This prolonged suppression of PV neurons by SOM neurons potentially allows a decrease of PV inhibitory input onto local excitatory populations, which in turn could amplify Off-R.

In summary, our results suggest that the spatial distribution of On and Off-R MGB terminals determines the spatial distribution of On-R or Off-R A1 neurons and that Off-Rs are amplified compared to On-Rs due to disinhibition through suppression of PV interneurons by SOM interneurons (Figure 7), as well as to increased local spatial clustering of Off-R MGB afferents (Figure 7G).

DISCUSSION

We show that ACX encodes tone offset in a parallel, spatially extensive, yet globally, tonotopically organized manner. We find distinct functional ACX areas characterized by distinct On and Off selectivity on the population level. Thus, the cortical representation of spectral information is influenced by the temporal

dynamics of spectrally static tones. GC analysis revealed that ACX areas contain intermingled On and Off networks within L2/3. Therefore, areal selectivity is due to both different numbers of On and Off-R neurons and distinct intracortical circuits. Distinct temporal dynamics in the responses of PV and SOM interneurons point to disinhibition as one mechanism that amplifies Off-R. Moreover, areal and cellular On and Off-R selectivity may arise from differences in MGB input, which could be enhanced by spatially correlated activity of MGB terminals. Altogether, our results suggest that the differential dynamic responses originate from differential feedforward input from MGB and are elaborated by different intrinsic excitatory and inhibitory circuits in different ACX regions. Thus, ACX areas operate in parallel to extract temporal information. Our results also demonstrate that Off-Rs are tonotopically organized on the mesoscale. The lack of Off-R tonotopy in prior studies (Baba et al., 2016) is likely due to Off-R being most prominent in awake animals (Fishman and Steinschneider, 2009; Joachimsthaler et al., 2014; Qin et al., 2007; Recanzone, 2000).

We here developed a method to define functional ACX areas based on temporal coactivation of pixels in the WF dataset (Whiteway and Butts, 2017). This method is unbiased and unsupervised, requires no prior knowledge of the locations of cortical fields, and can be applied to arbitrary WF datasets.

Besides tone onset and offset, ACX neurons can be sensitive to other dynamic aspects of sound, such as amplitude or frequency modulation, sound duration, and frequency sweep rate (Baumann et al., 2015; He et al., 1997; Heil et al., 1992; Issa et al., 2017; Schreiner and Urbas, 1986). While frequency sweep rate is topographically organized in mouse ACX (Issa et al., 2017), our results show that Off-Rs are also topographically represented.

We found an extensive representation of tone offset in A1 and DP neurons. A1 neurons receive On and Off synaptic inputs shown to be mediated by nonoverlapping sets of synapses (Scholl et al., 2010). We found that MGB terminals mostly have only On-Rs or Off-Rs, suggesting that A1 neurons receive convergent input from such On-R or Off-R MGB terminals. Furthermore, Off-R MGB terminals do not outnumber On-R MGB terminals and MGB terminals have weaker Off-R, suggesting that the cellular Off-R dominance in A1 results from different On and Off-R input topology, or the spatial distribution of connections. No evidence so far suggests that On and Off circuits have different quantal synaptic strength; thus, the cellular On and Off-R bias is more likely to result from differential convergence of connections. Altogether, these observations suggest the presence of local A1 circuits to amplify Off-R. Our results suggest that a disinhibitory circuit formed by SOM and PV cells could play this role. A multilayer nonlinear neural network has been proposed to underlie the various On and Off-Rs observed in A1 (Deneux et al., 2016). Our work suggests that the MGB-A1 circuit could underlie this transformation. Ideally, our conclusion would be strengthened by simultaneously imaging MGB terminals and ACX postsynaptic neurons. However, such an approach would be limited, because corresponding terminals and postsynaptic neurons would not necessarily be localized in the same imaging plane, making it difficult to determine unequivocally presynaptic terminal and postsynaptic cell pairs.

On-R and Off-R MGB terminals likely originate from different MGB subdivisions. ACX receives MGB inputs via lemniscal and nonlemniscal pathways. The lemniscal pathway arises from the ventral MGB (MGBv), which shows On-Rs (Aitkin and Webster, 1972; Hackett et al., 2011; Imig and Morel, 1983; Rediés and Brandner, 1991). Multiple lines of evidence suggest that Off-Rs originate in nonlemniscal pathways. Off-Rs are predominantly observed in a sheet partially surrounding MGBv (He, 2001). Off-Rs can also originate from the dorsal MGB (MGBd) and medial MGB (MGBm). We found that A2 and DP, which receive MGBd input (Lee and Sherman, 2008; Llano and Sherman, 2008) show Off-Rs. Moreover, the spatial extensiveness of Off-Rs is consistent with broad projection from MGBm to ACX through L1 (Huang and Winer, 2000; Lee and Winer, 2008). Thus, nonlemniscal pathways likely provide tone Off information to ACX. We imaged terminals at roughly the same depth as neurons (~150 μm); thus, these terminal might reflect a mixture of lemniscal and nonlemniscal pathways, because terminals from both MGBv and MGBd are present in L2 in A1 (Saldeitis et al., 2014). Our results show overlapping tonotopy of On-R and Off-R despite areal differences, suggesting that lemniscal and nonlemniscal pathways are coarsely aligned but show distinct spatial patterning.

Most responding A1 L2/3 neurons have either On-R or Off-R. Thus, the spatial heterogeneity of tonal responses in A1 L2/3 might be due to intermingled cells receiving differing thalamic inputs. In the primary somatosensory cortex (S1), functionally different thalamic inputs from the ventral posterior medial nucleus and the posterior medial nucleus are relayed to barrels and septa (Koralek et al., 1988; Lu and Lin, 1993), which are spatially separated and carry whisking-touch information (Yu et al., 2006) and temporal information on whisker movement, respectively (Ahissar et al., 2000). Our results suggest that in contrast to S1, functionally different thalamic inputs to A1 are spatially interspersed. A1 L2/3 contains cells with distinct functional intracortical circuits and shows a sublaminar organization (Meng et al., 2017). It is possible that the distinct On and Off subnetworks we identified relate to these distinct subpopulations. Because recurrent inputs from subgranular layers are thought to be able to amplify thalamic inputs (Li et al., 2013; Miller et al., 2001; Somers et al., 1995), we speculate that Off-R cells receive stronger or more extensive inputs from subgranular layers. Prior electrophysiology studies identified a larger proportion of neurons responding to both tone onset and offset (Joachimsthaler et al., 2014; Qin et al., 2007). The discrepancy most likely results from differences in recording depth and the inclusion of multiunit activity, given the intermingled spatial distribution of On-Rs and Off-Rs (Figure 5B), which could bias electrophysiological studies. Although our single-unit recordings (Figure S7) showed a significant proportion of neurons responding to both tone onset and offset, there was a differential distribution of Off-R bias across the depth of A1, with superficial A1 cells being more Off-R biased. Thus, Off-Rs are more prevalent in superficial layers, where we imaged (~150 μm depth). This is also consistent with the laminar targets of lemniscal and nonlemniscal MGB afferents, with the latter being present in L1 (Llano and Sherman, 2008; Saldeitis et al., 2014) and with L5/6 neurons less likely to generate Off-R (Volkov and Galazjuk, 1991).In

addition, L2/3 shows a functional suborganization (Meng et al., 2017), with deep L3b receiving L4 inputs and superficial L2a receiving few L4 inputs. Thus, it is likely the recurrent connections in L2a amplify the segregation of On and Off-R, as well as Off-R strength. Future studies linking intracortical connectivity with functional responses are needed to explore these issues. Altogether, given that two-photon imaging has much higher spatial resolution and lacks electrode bias, our imaging results most likely revealed a highly specific On and Off-R selectivity in upper L2/3.

We found that ~5% of neurons in A1 respond to tone onset and offset, consistent with a sparse representation of sound in rat A1 (Hromádka et al., 2008) and mouse A1 (Liang et al., 2018). However, previous imaging studies of A1 have reported a 20%–30% response rate (Issa et al., 2014; Kato et al., 2015). This discrepancy likely arises from sampling different neuronal populations. Issa et al. (2014) used cre-dependent GCaMP3 driven by Syn1-cre or Emx-cre. In the primary visual cortex (V1), such labeled populations had fewer visual responses compared with the Oregon green BAPTA-1 (OGB-1)-labeled neurons (Zariwala et al., 2012), suggesting nonuniform population labeling. Kato et al. (2015) used viral expression of GCaMP6s under a Syn1 promotor, which densely labeled neurons close to the injection site. We used the GP4.2 line, which relatively uniformly labels about 70% of L2/3 pyramidal cells (Dana et al., 2014). The difference in response rate between our and prior imaging studies is likely due to labeling of different but potentially overlapping populations, the difference in calcium indicator (GCaMP3 versus GCaMP6s), expression profile (transgenic versus viral expression), and cell selection or inclusion criteria.

We find that L2/3 PV and SOM interneurons show distinct temporal dynamics from each other, as well as from excitatory neurons. PV and SOM interneurons show mostly opposite signs of responses. Because the suppression of PV responses likely indicates a reduction in the firing rate (Forli et al., 2018), our data suggest suppression of PV activity by SOM interneurons, consistent with mostly suppressed responses of L2/3 PV neurons to prolonged tones (Kato et al., 2015) and the proposed cortical processing scheme of SOM → PV inhibition (Pfeffer et al., 2013). Finally, SOM neurons more readily inhibit PV neurons than they inhibit local excitatory neurons (Cottam et al., 2013). We speculate that such inhibition could facilitate detection of changes in auditory streams, such as tone offset. The duration of inhibitory postsynaptic currents in PV cells could outlast firing of SOM cells, creating a window for elevated excitability in local pyramidal cells before PV activity returns to baseline. Furthermore, we find that SOM cells are active throughout tone presentation, in contrast to previous findings that SOM cells fire transiently, although this difference could be due to the animal's state (Chen et al., 2015; Li et al., 2015). Thus, SOM cells are potentially important for auditory stream analysis, and their interactions with PV neurons could facilitate change detection.

In conclusion, we have demonstrated a distinctly extensive parallel spatial representation of sound dynamics in ACX at multiple levels, and we propose that this spatial pattern is determined by the meso- and microscale spatial layout of thalamic input and by distinct intracortical circuits.

STAR★METHODS

Detailed methods are provided in the online version of this paper and include the following:

- KEY RESOURCES TABLE
- CONTACT FOR REAGENT AND RESOURCE SHARING
- EXPERIMENTAL MODEL AND SUBJECT DETAILS
- METHOD DETAILS
  - Chronic window implant
  - Widefield imaging
  - Acoustic stimulus
  - 2-Photon imaging of mouse ACX
  - Injection of GCaMP6s virus in MGB
  - Pupillometry
  - Extracellular electrophysiology
- QUANTIFICATION AND STATISTICAL ANALYSIS
  - Widefield image preprocessing
  - Image Segmentation with constrained autoencoder
  - Widefield On-R and Off-R amplitude
  - Field Parcellation
  - Signal correlation among ROIs
  - On- and Off-tonotopy
  - 2-Photon imaging data analysis
  - Off-R Bias Index (OBI)
  - Granger Causality analysis
  - Pupillometry data analysis
  - Electrophysiological data analysis

SUPPLEMENTAL INFORMATION

Supplemental Information can be found online at https://doi.org/10.1016/j.celrep.2019.03.069.

ACKNOWLEDGMENTS

Supported by NIH RO1DC009607 (to P.O.K.), NSF 1552946 (to B.B.), NSF 1807216 (to B.B.), NIH T32DC00046 (M.R.W.), and NSF IIS-1350990 (to D.A.B.).

AUTHOR CONTRIBUTIONS

J.L. and P.O.K. designed the research. J.L. performed experiments and analyzed the data. M.R.W., D.A.B., and J.L. designed and implemented the autoencoder analysis algorithm. A.S. and B.B. implemented Granger analysis. P.O.K. supervised the research. J.L. and P.O.K. wrote the paper.

DECLARATION OF INTERESTS

The authors declare no competing interests.

Received: May 3, 2018
Revised: October 24, 2018
Accepted: March 18, 2019
Published: April 16, 2019

REFERENCES

Ahissar, E., Sosnik, R., and Haidarliu, S. (2000). Transformation from temporal to rate coding in a somatosensory thalamocortical pathway. Nature *406*, 302–306.

Aitkin, L.M., and Webster, W.R. (1972). Medial geniculate body of the cat: organization and responses to tonal stimuli of neurons in ventral division. J. Neurophysiol. *35*, 365–380.

Baba, H., Tsukano, H., Hishida, R., Takahashi, K., Horii, A., Takahashi, S., and Shibuki, K. (2016). Auditory cortical field coding long-lasting tonal offsets in mice. Sci. Rep. *6*, 34421.

Bandyopadhyay, S., Shamma, S.A., and Kanold, P.O. (2010). Dichotomy of functional organization in the mouse auditory cortex. Nat. Neurosci. *13*, 361–368.

Baumann, S., Joly, O., Rees, A., Petkov, C.I., Sun, L., Thiele, A., and Griffiths, T.D. (2015). The topography of frequency and time representation in primate auditory cortices. eLife *4*, e03256.

Bengio, Y., Courville, A., and Vincent, P. (2013). Representation learning: a review and new perspectives. IEEE Trans. Pattern Anal. Mach. Intell. *35*, 1798–1828.

Benjamini, Y., and Yekutieli, D. (2001). The control of the false discovery rate in multiple testing under dependency. Ann. Stat. *29*, 1165–1188.

Bregman, A.S. (1994). Auditory scene analysis: The perceptual organization of sound (MIT Press).

Bruno, R.M., and Sakmann, B. (2006). Cortex is driven by weak but synchronously active thalamocortical synapses. Science *312*, 1622–1627.

Chen, I.-W., Helmchen, F., and Lütcke, H. (2015). Specific early and late oddball-evoked responses in excitatory and inhibitory neurons of mouse auditory cortex. J. Neurosci. *35*, 12560–12573.

Cottam, J.C., Smith, S.L., and Häusser, M. (2013). Target-specific effects of somatostatin-expressing interneurons on neocortical visual processing. J. Neurosci. *33*, 19567–19578.

Dana, H., Chen, T.W., Hu, A., Shields, B.C., Guo, C., Looger, L.L., Kim, D.S., and Svoboda, K. (2014). Thy1-GCaMP6 transgenic mice for neuronal population imaging *in vivo*. PLoS ONE *9*, e108697.

Deneux, T., Kempf, A., Daret, A., Ponsot, E., and Bathellier, B. (2016). Temporal asymmetries in auditory coding and perception reflect multi-layered nonlinearities. Nat. Commun. *7*, 12682.

Fishman, Y.I., and Steinschneider, M. (2009). Temporally dynamic frequency tuning of population responses in monkey primary auditory cortex. Hear. Res. *254*, 64–76.

Forli, A., Vecchia, D., Binini, N., Succol, F., Bovetti, S., Moretti, C., Nespoli, F., Mahn, M., Baker, C.A., Bolton, M.M., et al. (2018). Two-Photon Bidirectional Control and Imaging of Neuronal Excitability with High Spatial Resolution *In Vivo*. Cell Rep. *22*, 3087–3098.

Francis, N.A., Winkowski, D.E., Sheikhattar, A., Armengol, K., Babadi, B., and Kanold, P.O. (2018). Small Networks Encode Decision-Making in Primary Auditory Cortex. Neuron *97*, 885–897.

Frisina, R.D., Singh, A., Bak, M., Bozorg, S., Seth, R., and Zhu, X. (2011). F1 (CBA×C57) mice show superior hearing in old age relative to their parental strains: hybrid vigor or a new animal model for "golden ears"? Neurobiol. Aging *32*, 1716–1724.

Friston, K., Moran, R., and Seth, A.K. (2013). Analysing connectivity with Granger causality and dynamic causal modelling. Curr. Opin. Neurobiol. *23*, 172–178.

Granger, C.W. (1969). Investigating causal relations by econometric models and cross-spectral methods. Econometrica *37*, 424–438.

Guo, W., Chambers, A.R., Darrow, K.N., Hancock, K.E., Shinn-Cunningham, B.G., and Polley, D.B. (2012). Robustness of cortical topography across fields, laminae, anesthetic states, and neurophysiological signal types. J. Neurosci. *32*, 9159–9172.

Hackett, T.A., Barkat, T.R., O'Brien, B.M., Hensch, T.K., and Polley, D.B. (2011). Linking topography to tonotopy in the mouse auditory thalamocortical circuit. J. Neurosci. *31*, 2983–2995.

He, J. (2001). On and off pathways segregated at the auditory thalamus of the guinea pig. J. Neurosci. *21*, 8672–8679.

He, J., Hashikawa, T., Ojima, H., and Kinouchi, Y. (1997). Temporal integration and duration tuning in the dorsal zone of cat auditory cortex. J. Neurosci. *17*, 2615–2625.

Heil, P., Rajan, R., and Irvine, D.R. (1992). Sensitivity of neurons in cat primary auditory cortex to tones and frequency-modulated stimuli. I: Effects of variation of stimulus parameters. Hear. Res. *63*, 108–134.

Henry, K.R. (1985). Tuning of the auditory brainstem OFF responses is complementary to tuning of the auditory brainstem ON response. Hear. Res. *19*, 115–125.

Herreras, O. (2016). Local field potentials: myths and misunderstandings. Front. Neural Circuits *10*, 101.

Hillyard, S.A., and Picton, T.W. (1978). On and off components in the auditory evoked potential. Percept. Psychophys. *24*, 391–398.

Hromádka, T., Deweese, M.R., and Zador, A.M. (2008). Sparse representation of sounds in the unanesthetized auditory cortex. PLoS Biol. *6*, e16.

Huang, C.L., and Winer, J.A. (2000). Auditory thalamocortical projections in the cat: laminar and areal patterns of input. J. Comp. Neurol. *427*, 302–331.

Imig, T.J., and Morel, A. (1983). Organization of the thalamocortical auditory system in the cat. Annu. Rev. Neurosci. *6*, 95–120.

Issa, J.B., Haeffele, B.D., Agarwal, A., Bergles, D.E., Young, E.D., and Yue, D.T. (2014). Multiscale optical Ca2+ imaging of tonal organization in mouse auditory cortex. Neuron *83*, 944–959.

Issa, J.B., Haeffele, B.D., Young, E.D., and Yue, D.T. (2017). Multiscale mapping of frequency sweep rate in mouse auditory cortex. Hear. Res. *344*, 207–222.

Ji, X.Y., Zingg, B., Mesik, L., Xiao, Z., Zhang, L.I., and Tao, H.W. (2016). Thalamocortical innervation pattern in mouse auditory and visual cortex: laminar and cell-type specificity. Cereb. Cortex *26*, 2612–2625.

Joachimsthaler, B., Uhlmann, M., Miller, F., Ehret, G., and Kurt, S. (2014). Quantitative analysis of neuronal response properties in primary and higher-order auditory cortical fields of awake house mice (*Mus musculus*). Eur. J. Neurosci. *39*, 904–918.

Kane, K.L., Longo-Guess, C.M., Gagnon, L.H., Ding, D., Salvi, R.J., and Johnson, K.R. (2012). Genetic background effects on age-related hearing loss associated with Cdh23 variants in mice. Hear. Res. *283*, 80–88.

Kanold, P.O., Nelken, I., and Polley, D.B. (2014). Local versus global scales of organization in auditory cortex. Trends Neurosci. *37*, 502–510.

Kato, H.K., Gillet, S.N., and Isaacson, J.S. (2015). Flexible sensory representations in auditory cortex driven by behavioral relevance. Neuron *88*, 1027–1039.

Katzner, S., Nauhaus, I., Benucci, A., Bonin, V., Ringach, D.L., and Carandini, M. (2009). Local origin of field potentials in visual cortex. Neuron *61*, 35–41.

Kim, S., Putrino, D., Ghosh, S., and Brown, E.N. (2011). A Granger causality measure for point process models of ensemble neural spiking activity. PLoS Comput. Biol. *7*, e1001110.

Kopp-Scheinpflug, C., Tozer, A.J., Robinson, S.W., Tempel, B.L., Hennig, M.H., and Forsythe, I.D. (2011). The sound of silence: ionic mechanisms encoding sound termination. Neuron *71*, 911–925.

Koralek, K.-A., Jensen, K.F., and Killackey, H.P. (1988). Evidence for two complementary patterns of thalamic input to the rat somatosensory cortex. Brain Res. *463*, 346–351.

Lee, C.C., and Sherman, S.M. (2008). Synaptic properties of thalamic and intracortical inputs to layer 4 of the first- and higher-order cortical areas in the auditory and somatosensory systems. J. Neurophysiol. *100*, 317–326.

Lee, C.C., and Winer, J.A. (2008). Connections of cat auditory cortex: I. Thalamocortical system. J. Comp. Neurol. *507*, 1879–1900.

Li, L.Y., Li, Y.T., Zhou, M., Tao, H.W., and Zhang, L.I. (2013). Intracortical multiplication of thalamocortical signals in mouse auditory cortex. Nat. Neurosci. *16*, 1179–1181.

Li, L.Y., Xiong, X.R., Ibrahim, L.A., Yuan, W., Tao, H.W., and Zhang, L.I. (2015). Differential receptive field properties of parvalbumin and somatostatin inhibitory neurons in mouse auditory cortex. Cereb. Cortex *25*, 1782–1791.

Liang, F., Li, H., Chou, X.L., Zhou, M., Zhang, N.K., Xiao, Z., Zhang, K.K., Tao, H.W., and Zhang, L.I. (2018). Sparse Representation in Awake Auditory Cortex: Cell-type Dependence, Synaptic Mechanisms, Developmental Emergence, and Modulation. Cereb. Cortex, Published online October 11, 2018. https://doi.org/10.1093/cercor/bhy260.

Liu, X., Zhou, L., Ding, F., Wang, Y., and Yan, J. (2015). Local field potentials are local events in the mouse auditory cortex. Eur. J. Neurosci. *42*, 2289–2297.

Llano, D.A., and Sherman, S.M. (2008). Evidence for nonreciprocal organization of the mouse auditory thalamocortical-corticothalamic projection systems. J. Comp. Neurol. *507*, 1209–1227.

Lu, S.-M., and Lin, R.C.-S. (1993). Thalamic afferents of the rat barrel cortex: a light- and electron-microscopic study using Phaseolus vulgaris leucoagglutinin as an anterograde tracer. Somatosens. Mot. Res. *10*, 1–16.

Maor, I., Shalev, A., and Mizrahi, A. (2016). Distinct spatiotemporal response properties of excitatory versus inhibitory neurons in the mouse auditory cortex. Cereb. Cortex *26*, 4242–4252.

McGinley, M.J., David, S.V., and McCormick, D.A. (2015). Cortical membrane potential signature of optimal states for sensory signal detection. Neuron *87*, 179–192.

Meng, X., Winkowski, D.E., Kao, J.P.Y., and Kanold, P.O. (2017). Sublaminar subdivision of mouse auditory cortex layer 2/3 based on functional translaminar connections. J. Neurosci. *37*, 10200–10214.

Merzenich, M.M., Knight, P.L., and Roth, G.L. (1975). Representation of cochlea within primary auditory cortex in the cat. J. Neurophysiol. *38*, 231–249.

Miller, K.D., Pinto, D.J., and Simons, D.J. (2001). Processing in layer 4 of the neocortical circuit: new insights from visual and somatosensory cortex. Curr. Opin. Neurobiol. *11*, 488–497.

Oya, H., Poon, P.W., Brugge, J.F., Reale, R.A., Kawasaki, H., Volkov, I.O., and Howard, M.A., 3rd. (2007). Functional connections between auditory cortical fields in humans revealed by Granger causality analysis of intra-cranial evoked potentials to sounds: comparison of two methods. Biosystems *89*, 198–207.

Pachitariu, M., Stringer, C., Schröder, S., Dipoppa, M., Rossi, L.F., Carandini, M., and Harris, K.D. (2016). Suite2p: beyond 10,000 neurons with standard two-photon microscopy. bioRxiv. https://doi.org/10.1101/061507.

Petrus, E., Isaiah, A., Jones, A.P., Li, D., Wang, H., Lee, H.-K., and Kanold, P.O. (2014). Crossmodal induction of thalamocortical potentiation leads to enhanced information processing in the auditory cortex. Neuron *81*, 664–673.

Pfeffer, C.K., Xue, M., He, M., Huang, Z.J., and Scanziani, M. (2013). Inhibition of inhibition in visual cortex: the logic of connections between molecularly distinct interneurons. Nat. Neurosci. *16*, 1068–1076.

Polley, D.B., Read, H.L., Storace, D.A., and Merzenich, M.M. (2007). Multiparametric auditory receptive field organization across five cortical fields in the albino rat. J. Neurophysiol. *97*, 3621–3638.

Qin, L., Chimoto, S., Sakai, M., Wang, J., and Sato, Y. (2007). Comparison between offset and onset responses of primary auditory cortex ON-OFF neurons in awake cats. J. Neurophysiol. *97*, 3421–3431.

Recanzone, G.H. (2000). Response profiles of auditory cortical neurons to tones and noise in behaving macaque monkeys. Hear. Res. *150*, 104–118.

Redies, H., and Brandner, S. (1991). Functional organization of the auditory thalamus in the guinea pig. Exp. Brain Res. *86*, 384–392.

Rose, T., Jaepel, J., Hübener, M., and Bonhoeffer, T. (2016). Cell-specific restoration of stimulus preference after monocular deprivation in the visual cortex. Science *352*, 1319–1322.

Rothschild, G., Nelken, I., and Mizrahi, A. (2010). Functional organization and population dynamics in the mouse primary auditory cortex. Nat. Neurosci. *13*, 353–360.

Saldeitis, K., Happel, M.F., Ohl, F.W., Scheich, H., and Budinger, E. (2014). Anatomy of the auditory thalamocortical system in the Mongolian gerbil: nuclear origins and cortical field-, layer-, and frequency-specificities. J. Comp. Neurol. *522*, 2397–2430.

Schmidt, M., Berg, E., Friedlander, M., and Murphy, K. (2009). Optimizing costly functions with simple constraints: A limited-memory projected quasi-newton algorithm. Proc. Mach. Learn. Res. *5*, 456–463.

Scholl, B., Gao, X., and Wehr, M. (2010). Nonoverlapping sets of synapses drive on responses and off responses in auditory cortex. Neuron *65*, 412–421.

Schreiner, C.E., and Urbas, J.V. (1986). Representation of amplitude modulation in the auditory cortex of the cat. I. The anterior auditory field (AAF). Hear. Res. *21*, 227–241.

Shadlen, M.N., and Newsome, W.T. (1998). The variable discharge of cortical neurons: implications for connectivity, computation, and information coding. J. Neurosci. *18*, 3870–3896.

Sheikhattar, A., and Babadi, B. (2016). Dynamic estimation of causal influences in sparsely-interacting neuronal ensembles. In Proceedings of the 2016 IEEE Annual Conference on Information Science and Systems (CISS), pp. 551–556.

Sheikhattar, A., Miran, S., Liu, J., Fritz, J.B., Shamma, S.A., Kanold, P.O., and Babadi, B. (2018). Extracting neuronal functional network dynamics via adaptive Granger causality analysis. Proc. Natl. Acad. Sci. USA *115*, E3869–E3878.

Somers, D.C., Nelson, S.B., and Sur, M. (1995). An emergent model of orientation selectivity in cat visual cortical simple cells. J. Neurosci. *15*, 5448–5465.

Stiebler, I., Neulist, R., Fichtel, I., and Ehret, G. (1997). The auditory cortex of the house mouse: left-right differences, tonotopic organization and quantitative analysis of frequency representation. J. Comp. Physiol. A Neuroethol. Sens. Neural Behav. Physiol. *181*, 559–571.

Thévenaz, P., Ruttimann, U.E., and Unser, M. (1998). A pyramid approach to subpixel registration based on intensity. IEEE Trans. Image Process. *7*, 27–41.

Tian, B., Kuśmierek, P., and Rauschecker, J.P. (2013). Analogues of simple and complex cells in rhesus monkey auditory cortex. Proc. Natl. Acad. Sci. USA *110*, 7892–7897.

Tsukano, H., Horie, M., Bo, T., Uchimura, A., Hishida, R., Kudoh, M., Takahashi, K., Takebayashi, H., and Shibuki, K. (2015). Delineation of a frequency-organized region isolated from the mouse primary auditory cortex. J. Neurophysiol. *113*, 2900–2920.

Valdés-Sosa, P.A., Sánchez-Bornot, J.M., Lage-Castellanos, A., Vega-Hernández, M., Bosch-Bayard, J., Melie-García, L., and Canales-Rodríguez, E. (2005). Estimating brain functional connectivity with sparse multivariate autoregression. Philos. Trans. R. Soc. Lond. B Biol. Sci. *360*, 969–981.

Vasquez-Lopez, S.A., Weissenberger, Y., Lohse, M., Keating, P., King, A.J., and Dahmen, J.C. (2017). Thalamic input to auditory cortex is locally heterogeneous but globally tonotopic. eLife *6*, e25141.

Volkov, I.O., and Galazjuk, A.V. (1991). Formation of spike response to sound tones in cat auditory cortex neurons: interaction of excitatory and inhibitory effects. Neuroscience *43*, 307–321.

Whiteway, M.R., and Butts, D.A. (2017). Revealing unobserved factors underlying cortical activity with a rectified latent variable model applied to neural population recordings. J. Neurophysiol. *117*, 919–936.

Winkowski, D.E., and Kanold, P.O. (2013). Laminar transformation of frequency organization in auditory cortex. J. Neurosci. *33*, 1498–1508.

Yu, C., Derdikman, D., Haidarliu, S., and Ahissar, E. (2006). Parallel thalamic pathways for whisking and touch signals in the rat. PLoS Biol. *4*, e124.

Zariwala, H.A., Borghuis, B.G., Hoogland, T.M., Madisen, L., Tian, L., De Zeeuw, C.I., Zeng, H., Looger, L.L., Svoboda, K., and Chen, T.-W. (2012). A Cre-dependent GCaMP3 reporter mouse for neuronal imaging *in vivo*. J. Neurosci. *32*, 3131–3141.

STAR★METHODS

KEY RESOURCES TABLE

REAGENT or RESOURCE	SOURCE	IDENTIFIER
Bacterial and Virus Strains		
AAV1.Syn.Flex.mRuby2.GSG.P2A.GCaMP6s.WPRE.SV40	(Rose et al., 2016)	Addgene 68720-AAV1
Experimental Models: Organisms/Strains		
Mouse: C57BL/6J-Tg(Thy1-GCaMP6s)GP4.3Dkim/J	The Jackson Laboratory	JAX 024275
Mouse: CBA/CaJ	The Jackson Laboratory	JAX 000654
Mouse: B6;129P2-Pvalb$^{tm1(cre)Arbr}$/J	The Jackson Laboratory	JAX 008069
Mouse: Sst$^{tm2.1(cre)Zjh}$/J	The Jackson Laboratory	JAX 013044
Software and Algorithms		
Autoencoder	(Whiteway and Butts, 2017)	https://github.com/themattinthehatt/rlvm
Suite2P	(Pachitariu et al., 2016)	https://github.com/cortex-lab/Suite2P
TurboReg	(Thévenaz et al., 1998)	http://bigwww.epfl.ch/thevenaz/turboreg/
MClust3.5	A. David Redish	http://redishlab.neuroscience.umn.edu/MClust/MClust.html
Klustakwik	Ken Harris	http://klustakwik.sourceforge.net/

CONTACT FOR REAGENT AND RESOURCE SHARING

Further information and requests for resources and reagents should be directed to and will be fulfilled by the Lead Contact, Patrick Kanold (pkanold@umd.edu).

EXPERIMENTAL MODEL AND SUBJECT DETAILS

All procedures were approved by the University of Maryland's Animal Care and Use Committee. We crossed CBA/CaJ (JAX stock #000654) mice with Thy1-GCaMP6s (JAX stock #024275, GP4.3, (Dana et al., 2014)) to obtain F1's since C57BL/6 are homozygous for Cdh23 allele ahl, which causes them to suffer from aging related hearing loss, while CBA/CaJ mice are homozygous for Ahl+, which spare them from the phenotype (Kane et al., 2012). F1's thus have no hearing loss and yet have uniform expression of GCaMP6s under Thy1 promotor in excitatory neurons. We used adult mice of both sexes whose ages range from 2 to 4 months old. For imaging PV or SOM neurons, we crossed Thy1-GCaMP6s mice with PV-cre (JAX #008069) or SOM-cre (JAX #013044) mice and injected ~30nl of AAV1.Syn.Flex.mRuby2.GSG.P2A.GCaMP6s.WPRE.SV40 (Addgene viral prep # 68720-AAV1 (Rose et al., 2016)) into the left ACX of the F1 animals. Such generated animals express innate GCaMP6s in Thy1 pyramidal cells while expressing GCaMP6s and mRuby in either PV and SOM interneurons.

METHOD DETAILS

Chronic window implant

2-3 hours before surgery, 0.1cc dexamethasone (2mg/ml, VetOne) was injected subcutaneously to reduce brain swelling during craniotomy. Anesthesia was induced with 4% isoflurane (Fluriso, VetOne) with a calibrated vaporizer (Matrx VIP 3000). During surgery, isoflurane level was reduced to and maintained at a level of 1.5%–2%. Body temperature of the animal was maintained at 36.0°C during surgery. Hair on top of head of the animal was removed using Hair Remover Face Cream (Nair), after which Betadine (Purdue Products) and 70% ethanol was applied sequentially 3 times to the surface of the skin before the central part is removed. Soft tissues and muscles were scraped to expose the skull. Then a custom designed 3D printed stainless headplate was mounted over the left auditory cortex and secured with C&B-bond (Parkell). A craniotomy with a diameter of about 3.5mm was then performed over the left auditory cortex. A three layered coverslip was used as cranial window, which is made by stacking 2 pieces of 3mm coverslips (64-0720 (CS-3R), Warner Instruments) at the center of a 5mm coverslip (64-0700 (CS-5R), Warner Instruments), using optic glue (NOA71, Norland Products). The cranial window was quickly dabbed in kwik-sil (World Precision Instruments) before mounted onto the brain with 3mm coverslips facing down. After kwik-sil cured (2-5min), C&B-bond was applied to secure the cranial window. Synthetic black iron oxide (Alpha Chemicals) was then applied to the hardened surface. 0.05cc Cefazolin (1 g/vial, West Ward Pharmaceuticals) was

injected subcutaneously when the entire procedure was finished. After the surgery, the animal was kept warm under heat light for 30 minutes for recovery before returning to the home cage. Medicated water (Sulfamethoxazole and Trimethoprim Oral Suspension, USP 200mg/40mg per 5ml, Aurobindo Pharms USA; 6ml solution diluted in 100ml water) substituted normal drinking water for 7 days before any imaging was performed.

Widefield imaging

Mice were affixed to a custom designed head-post and restrained within a plastic tube. The head of the animal was held upright. Imaging was performed using Ultima-IV two photon microscope (Bruker Technologies) with an orbital nosepiece such that the illuminance light is roughly perpendicular to cranial window (rotation angle was ~60 degrees). As a result, the anterior-posterior axis was not parallel to the edge of the images. 470nm LED light (M470L3, Thorlabs Inc.) was used to excite green fluorescence. Images were acquired with StreamPix 6.5 software (Norpix) at 10Hz and 100ms exposure time. In StreamPix software, we specified the image size to be 400 by 400 with a spatial binning of 3.

Acoustic stimulus

Pure tones were generated with custom MATLAB scripts. Each tone lasted 2 s with linear ramps of 5ms at the beginning and at the end of the tone. The amplitudes of the tones were calibrated to 75dB SPL with a Brüel & Kjær 4944-A microphone. During sound presentation, sound waveform was loaded into RX6 multi-function processor (Tucker-Davis Technologies (TDT)) and attenuated to desired sound levels by PA5 attenuator (TDT). Then the signal was fed into ED1 speaker driver (TDT), which drove an ES1 electrostatic speaker (TDT). The speaker was placed on the right-hand side of the animal, 10cm away from the head, at an angle of 45 degrees relative to the mid-line. The presentation of tones with various combination of frequencies and sound levels are randomized and controlled by a custom MATLAB program. The silent period in between the 2 s tones was randomly chosen from a uniform distribution between 3 and 3.5 s. Frequencies of the tones vary from 4kHz to 83.0kHz with logarithmic spacing and with a density of 2.28 tones per octave. Sound levels vary from 5dB SPL to 65dB SPL with a step of 15dB. Each stimulus was repeated 10 times. In total, the widefield imaging session for for each animal lasted ~45min. For 2-photon imaging, 9 tones with equal logarithmic spacing between 4 and 64kHz were used at a single level of 60dB SPL. The tone duration was 2 s and repeated 10 times.

2-Photon imaging of mouse ACX

A week after the cranial window implant, the animals were head-fixed in custom designed holder while 2 s long tones were presented in a similar fashion as in WF experiment. Field of views were placed in A1, AAF, A2 and DP region with a depth of around 150μm and with a size of 369 μm x 369 μm. The imaging was performed with a B-SCOPE (Thorlabs Inc.) with the microscope body tilted around 45 to 50 degrees while the mouse head was held upright. The excitation wavelength was 920nm and images were collected with ThorImage software (Thorlabs Inc.) at a frame rate of 30Hz. A 16x Nikon objective was used (NA 0.80). For terminal imaging, the average imaging depth was around 140um, comparable to cellular data.

Injection of GCaMP6s virus in MGB

AAV1.hSyn1.mRuby2.GSG.P2A.GCaMP6s.WPRE.SV40 (Addgene 50942) virus was injected into MGB for axon terminal imaging in ACX. Micropipettes pulled with a long tapering tip (> 3mm) were used for injection with Nanoject II (Drummond Inc.). The location of the left MGB was determined using the mouse brain atlas (AP: 3.2mm; ML 2.1mm; DV: 3.0mm). Anesthesia was induced with 4% isoflurane and maintained at 1.5%. The skin over the skull was cut open and a small craniotomy was made to allow penetration from the dorsal side and the micropipette was lowered vertically into MGB. 150-200nl of undiluted virus was injected over 5min. After the injection, the skin was sutured back. 3-4 weeks after the injection, the cranial window was implanted over the left ACX as previously described.

Pupillometry

During 2P imaging, the arousal state of the animal was monitored through pupillometry (McGinley et al., 2015). In short, a camera (BCE-B013-U, Mightex) was positioned around 20cm away from and toward the right eye of the head-fixed mouse. An ultraviolet LED was placed near the camera to restrict the pupil dilation to around 1/2 of the maximum dilation. The exposure time of the camera was set to 26ms and each frame was triggered by 2P "Frame Out" triggers and thus synchronized to 2P images.

Extracellular electrophysiology

We performed extracellular electrophysiology in CBA/CaJ and Thy1-GCaMP6s F1 crosses by either acutely recording from A1 neurons or chronically implanting electrodes. We used 16-channel linear arrays with 50μm spacing between adjacent contacts (A1x16-3mm-100-177-CM16, NeuroNexus) and a Neuralynx Cheetah system (32 channels). The acute surgery or implant surgery was similar to the cranial window implantations. In both cases, we first identified the location of A1 through widefield imaging of GCaMP6s and we advanced the electrode at a depth of around 900μm, which was read out from the manipulator. Figures S7A–S7E used data from chronic implantation while Figures S7F and S7G used single unit data pooling from both acute and chronic recordings. LFP signals and single units were acquired a previously described (Petrus et al., 2014). Briefly LFPs were acquired at 30kHz (filtered between 1 and 6000Hz) and down-sampled by a factor of 100 (using MATLAB built-in function 'decimate') before analysis. To calculate local

field potential (LFP) responses, we took the difference of the mean LFP amplitude within a 50ms time window before and after tone onset/offset. To determine the significance, we used a paired t test separately for each frequency and onset/offset and a significant change above baseline was considered a significant response. For spike extraction, the raw headstage signal was filtered from 300Hz to 6000Hz and detected online with a threshold of 30μv.

QUANTIFICATION AND STATISTICAL ANALYSIS

Widefield image preprocessing

We performed three preprocessing steps before using autoencoder for image segmentation. First, we downsampled the original image (400 by 400) using MATLAB (2015b) using the MATLAB built-in function 'imresize', by a factor of 4. The resultant image size was 100 by 100. Next we performed whitening of the image sequence. We first re-shaped each image into column vectors, then we stacked them horizontally. Let I_t denote the column vector corresponding to image at time t, M be the stacked matrix, and N be the total number of images:

$$M = [I_1, I_2, \cdots, I_N]$$

We then subtracted the time average image ($\langle I \rangle_t$) from all images:

$$\widehat{M} = M - \langle I \rangle_t \times \underbrace{[1,\ 1,\ \ldots,\ 1]}_{N}$$

We then performed singular value decomposition on sample covariance matrix of $\widehat{M}$:

$$[U, S, V] = SVD\left(\widehat{M} \times \widehat{M}^{'} \Big/ N\right)$$

Then we obtained the whitened images using the following equation:

$$\tilde{M} = U \times \left(S^{-1} + \lambda\right) \times U^{'} \times \widehat{M}$$

Where λ is the regularization term. We picked λ by first plotting the sorted eigenvalues in S in logarithmic space and usually a fast initial drop off and a following relatively flat region can be observed. We picked λ close to the turning point to preserve relevant variance and to avoid amplifying noise. We then fed $\tilde{M}$ into autoencoder algorithm.

Image Segmentation with constrained autoencoder

We used a dimensionality reduction technique to perform automatic image segmentation such that pixels with strong temporal correlations across the set of images were grouped together into single components (ROIs), following the formulation of Whiteway and Butts (2017). To perform this dimensionality reduction, we used an autoencoder neural network. The goal of this constrained autoencoder is to adjust the weights between the input layer and the hidden layer and those between the hidden layer and the output layer such that the output matches the input as closely as possible. For each time point t, the autoencoder takes the vector of pixel values $\mathbf{y}_t \in \mathbb{R}^N$ and projects it down onto a lower dimensional space $\mathbb{R}^M$ using an *encoding matrix* $\mathrm{W}_1 \in \mathbb{R}^{M \times N}$. A bias term $\mathbf{b}_1 \in \mathbb{R}^M$ is added to this projected vector, so that the resulting vector $\mathbf{z}_t \in \mathbb{R}^M$ is given by

$$\mathbf{z}_t = \mathrm{W}_1 \mathbf{y}_t + \mathbf{b}_1$$

The autoencoder then reconstructs the original activity $\mathbf{y}_t$ by applying a *decoding matrix* $\mathrm{W}_2 \in \mathbb{R}^{N \times M}$ to $\mathbf{z}_t$ and adding a bias term $\mathbf{b}_2 \in \mathbb{R}^N$, so that the reconstructed activity $\widehat{\mathbf{y}}_t \in \mathbb{R}^N$ is given by

$$\widehat{\mathbf{y}}_t = \mathrm{W}_2 \mathbf{z}_t + \mathbf{b}_2$$

Since the dimensionality of $\mathbf{z}_t$ is typically much smaller than that of $\mathbf{y}_t$, $\mathbf{z}_t$ should capture variations in $\mathbf{y}_t$ that are shared across many pixels. The entries of W_2 then describe how each pixel is related to each dimension of $\mathbf{z}_t$ (see Figure 2C).

The weight matrices and bias terms, grouped as $\Theta = [\mathrm{W}_1, \mathrm{W}_2, \mathbf{b}_1, \mathbf{b}_2]$, are simultaneously fit by minimizing the mean square error between the observed activity $\mathbf{y}_t$ and the predicted activity $\widehat{\mathbf{y}}_t$:

$$\widehat{\Theta} = \underset{\Theta}{\operatorname{argmin}} \frac{1}{2} \sum_t \mathbf{y}_t - \widehat{\mathbf{y}}_{t2}^2$$

To further enable interpretability of the results, we constrained the weights W_2 to be non-negative, as one could flip the signs of both spatial and temporal components arbitrarily. This also ensured that all pixels in a given ROI always increase or decrease in intensity together, depending on the sign of $\mathbf{z}_t$. We also tied the weights such that $\mathrm{W}_2 = \mathrm{W}_1^T$. Thus, there was essentially only one spatial weight matrix.

This version of the autoencoder is closely related to principal components analysis (PCA) (Bengio et al., 2013). However, PCA is an inadequate technique for automatic image segmentation since it did not in general result in spatially localized ROIs, due to the

orthogonality constraints imposed by the PCA model. A similar approach to our non-negatively constrained autoencoder is to use non-negative matrix factorization (NNMF) on the preprocessed image sequence. NNMF constrains both the spatial maps and the temporal activations to be non-negative, whereas the RLVM just constrains the spatial maps to be non-negative. The NNMF ROIs also failed to be spatially localized. Finally, in order to solve the constrained minimization problem above we used the spectral projected gradient method, a constrained variant of gradient descent (Schmidt et al., 2009).

To perform image segmentation with this method we must first specify the number of ROIs (the dimensionality of $\mathbf{z}_t$). We determined the appropriate number of ROIs using cross-validation by first fitting the parameters of the autoencoder on 75% of the frames from the image sequence (training data), and then reconstructing the remaining 25% of the images (testing data) using the autoencoder. We then calculated the correlation between the true and reconstructed images on the testing data, as a measurement for goodness of fit. In Figure S3A, we show that with an increasing number of ROIs, the correlation from the testing data increases monotonically, and roughly plateaus after ~50 ROIs. We also performed fitting on the entire image sequence and plot the correlation (Figure S3A, blue curve). A similar monotonic increase is observed, and with 50 or more ROIs, the correlation value is above 0.8, which is agreeable considering that the full image sequence consisted of more than 28,000 images. Another criterion we utilized to choose the number of ROIs was the total spatial area covered by the ROIs. An increasing portion of the total area is covered with an increasing number of ROIs, (Figure S3B), and total area covered by 50 ROIs are close to maximum coverage. Given these results, we typically used 50 ROIs in the autoencoder.

Widefield On-R and Off-R amplitude

To determine response amplitude, first the temporal trace from each trial was normalized to percentage change with respect to baseline fluorescence:

$$\text{normalized trace at time t} = F_t - F_0 / F_0$$

where F_0 is the baseline determined by finding the most frequent value in the histogram of the trace assuming stability. For On-R amplitude, we averaged the normalized trace from 200-500ms after tone onset with the baseline from normalized trace subtracted. For Off-R, we averaged the normalized trace from 200-500ms after tone offset and subtracted the average from the same trace 0-200ms right before tone offset. The 200-500ms window was sufficient to capture the rising phase as well as the peak of the increase in fluorescence in typical On/Off-R.

Field Parcellation

We assigned ROIs to different ACX fields based upon known tonotopic structure revealed with optical approaches (Issa et al., 2014; Tsukano et al., 2015). ACX of mice contains several ACX fields, including A1, AAF and Ultrasonic Field (UF), which are characterized by the presence of tonotopic gradients in On-R (Stiebler et al., 1997). Tonotopy also exists in secondary area A2, albeit on a compressed scale (Issa et al., 2014). First, we identified A1 and UF ROIs based on their two tonotopic axes, one from the caudal side to dorsomedial side (low to high) and the other one, sharing the same low frequency area, from caudal to ventrolateral side (Issa et al., 2014). The example A1 and UF ROIs (Figures 2I–2O) show progression of frequency selectivity along the two tonotopic axes. We use 'UF' and 'high A1' to distinguish between the two spatially distinct areas that are high frequency selective, while they are both considered primary auditory cortices. We also found a subset of ROIs located dorsoposterior to A1 which we assigned as DP. They showed relatively weak On-Rs but prominent Off-Rs (Figure 2M). We performed parcellation of ROIs in all animals studied, and the similar spatial layout of A1, UF, AAF, A2 and DP can be robustly observed.

Signal correlation among ROIs

We used corrected signal correlation (SC) for all our calculation due to the limited number of repeats and the strong tendency of close-by pixels to covary in time (Rothschild et al., 2010; Winkowski and Kanold, 2013). The basic idea is that the uncorrected SC equation contains products of responses from the two ROIs in question on the same trial, and these terms also appear in noise correlation equation. Thus, these products represent to some extent the covariation of ROIs regardless of stimulus presentation, and thus should be excluded from SC calculation. The denominator in the equation was adjusted accordingly to take into account the reduction of number of summation in the nominator.

In Figures 3G and 3H, we calculated SC among selected ROIs that were dorsally located with respect to A1 and UF respectively. These ROIs have centers within ~450μm to the A1 and UF ROIs in the rostrocaudal direction but dorsally located. Then we calculated pairwise SCs among all these ROI pairs and plotted them as a function of distance (Figure 3I).

On- and Off-tonotopy

To establish On- and Off-tonotopy, threshold of WF On-R and Off-R were first manually determined (Figure S1, white solid lines). Then WF images with baseline subtracted following tone onset or offset were obtained at identified threshold. Next a homomorphic filter was applied to the images to correct for unevenness of illumination. Then 95 percentile contour lines of the responses were extracted and overlaid to demonstrate systematic movement of activation area as a function of different tone frequencies (Figures 1C and 1D; Figure S3).

2-Photon imaging data analysis

First motion correction was performed with TurboReg plugin (Thévenaz et al., 1998). In a subset of experiments, the motion correction was performed using the Suite2P package (Pachitariu et al., 2016). ROIs were drawn manually using a custom written GUI. A ring was placed on each cell soma to extract raw fluorescence trace while a circular region of 20μm radius was used to extract nearby neuropil signal (excluding soma). We used the following equation to correct neuropil contamination of cell:

$$F_{corrected}(t) = F_{cell}(t) - 0.8 \times F_{neuropil}(t)$$

The coefficient of correction (0.8) was measured with the collected 2P dataset by taking the ratio of the intensity non-radial blood vessel and the intensity of adjacent neuropil containing no neurons. To calculate ΔF/F, the baseline of each cell was determined by constructing a histogram of all fluorescence intensity over time and by finding the peak of the histogram and the corresponding fluorescence intensity value, which we used as the estimate of fluorescence baseline. This procedure is based on several assumptions. First, we assume the baseline is constant over time, which we generally found to be true given our relatively short imaging sessions (~9 min). Second, we assume that the response in ACX is sparse (Hromádka et al., 2008) and thus baseline value should be observed the most often, which will be reflected as the peak in histogram. This procedure is generally robust and generates ΔF/F change over a reasonable range. If this procedure found negative baseline values, suggesting the soma fluorescence was lower in intensity than surrounding neuropil, then these cells were excluded from further analysis. Then, we calculate ΔF/F using the following equation:

$$\frac{\Delta F}{F}(t) = \frac{F_{corrected}(t) - baseline}{baseline}$$

To determine whether a cell is significantly responding to sound onset or offset, we first determine the response amplitude in the ΔF/F trace by finding the maximum change within 1 s after sound onset or offset and average over a small window (±2 frames) around the maximum time point to account for the noisy fluctuation in the trace. Then the 95 percent confidence interval (CI) of the median of the response amplitude was constructed through a bootstrapping procedure (resampling 1000 times) and if the lower CI bound exceeded 1.5 times the standard deviation of the baseline fluctuation (5 frames or ~150ms before sound onset/offset) then the cell was considered significantly on/off-responsive. The response significance was determined separately for each frequency and sound level combination and separately for On-R- and Off-R. Neuropil and MGB terminal signals were processed with the same procedure. Unlike cellular ROIs, MGB terminal ROIs were obtained with Suite2P in an automated fashion.

For classifying different types of responses (Figure 7E), we performed k-means clustering on averaged responses (across repetitions) to each frequency, pooling these traces from Thy1 (including traces from F1s of CBA/CaJ and Thy1-GCaMP6s crosses), PV and SOM neurons. The clustering is only confined to statistically significant responses. We used correlation as the distance measure and thus the clustering disregarded absolute amplitude of the traces. We chose 5 clusters to sufficiently encompass the different response types encountered.

Off-R Bias Index (OBI)

OBIs are calculated by first averaging On-R and Off-R for responding neurons over frequency and repeats, and then calculated with the following equation:

$$OBI = \frac{\langle R_{off} \rangle - \langle R_{on} \rangle}{\langle R_{off} \rangle + \langle R_{on} \rangle}$$

where the angle brackets denote average over tone frequency and repeats.

Granger Causality analysis

The notion of causality proposed by Granger (Granger, 1969) aims at capturing the two fundamental principles of temporal predictability and the precedence of cause over effect. In order to capture the functional dependencies within a neuronal ensemble and the sparsity of interactions, we employ sparse multivariate autoregressive models. We introduce a measure of GC which accounts for sparse interactions, estimate the model parameters using fast optimization methods, and perform statistical tests to assess the significance of possible GC interactions (Francis et al., 2018), while controlling the false discovery rate (FDR) to avoid spurious detection of GC links.

We used the same framework as in (Francis et al., 2018) for our Granger Causality (GC) measurement (Sheikhattar and Babadi, 2016). In order to infer GC patterns for the two On/Off conditions, we divide the corresponding responses to the onset and offset inputs, and pool across all the tone frequencies, thereby treating them as implicit repetitions to the same stimuli condition. In what follows, we present our modeling, parameter estimation and GC inference procedure.

Modeling: Consider a sequence of calcium indicator fluorescence measurements from a set of C neurons indexed by $c = 1, 2, \ldots, C$ within a slice, denoted by $\{y_{r,n}^{(c)}\}_{r=1:R, n=1:N}^{c=1:C}$ over time bins $n = 1,\ldots,N$, and across R trial repetitions indexed by $r = 1,\ldots,R$. We adopt a sparse vector autoregressive (VAR) framework (Valdés-Sosa et al., 2005) for modeling the slow-decaying and transient dynamics of the calcium fluorescence signals as well as the cross-dependencies among the neurons.

Suppose that the fluorescence observation vector of neuron (c) at the r-th repetition is represented by $\mathbf{y}_r^{(c)} := [y_{r,1}^{(c)}, \ldots, y_{r,N}^{(c)}]'$, and let $\overline{\mathbf{y}}^{(c)} := [\mathbf{y}_1^{(c)'}, \mathbf{y}_2^{(c)'}, \ldots, \mathbf{y}_R^{(c)'}]'$ denote the zero-mean total observation vector, containing the set of all observation vectors $\mathbf{y}_r^{(c)}$ from all trials $r = 1, \ldots, R$.

The effective neural covariates taken into account in our models are each neuron's self-history of activity and the history of activities of other neurons in the ensemble. We consider a lag of L samples within which the possible neuronal interactions may occur. Then, we segment L into M windows of lengths $W_1, W_2, \cdots, W_M$ such that $\sum_{i=1}^{M} W_i = L$. Let $b_m := \sum_{\ell=1}^{m} W_\ell$ for $m = 1, \ldots, M$, and $b_0 = 0$. Let

$$h_{r,n,m}^{(c)} := \frac{1}{W_m} \sum_{k=n-1-b_{m-1}}^{n-1-b_m} y_{r,k}^{(c)}, \tag{1}$$

represent the average activity of neuron (c) within the m-th window lag of length W_m with respect to time n and at trial r. We can then define the vector of history covariates from neuron (c), effective at time n and trial r as $\mathbf{h}_{r,n}^{(c)} := [h_{r,n,1}^{(c)}, h_{r,n,2}^{(c)}, \cdots, h_{r,n,M}^{(c)}]$. Next, let $\mathbf{x}_{r,n} := [\mathbf{h}_{r,n}^{(1)'}, \mathbf{h}_{r,n}^{(2)'}, \ldots, \mathbf{h}_{r,n}^{(C)'}]$ denote the vector of covariates from all neurons at time n and trial r.

In order to represent the covariates in a more compact form, we consider the $N \times MC$ matrix $\mathbf{X}_r := [\mathbf{x}_{r,1}, \mathbf{x}_{r,2}, \ldots, \mathbf{x}_{r,N}]'$ which contains in its rows the covariate vectors at all times $n = 1, \ldots, N$ within trial r. Finally, let $\overline{\mathbf{X}} := [\mathbf{X}_1', \mathbf{X}_2', \ldots, \mathbf{X}_R']$ represent the matrix of all covariates with standardized columns (i.e., zero-mean columns with unit norm), capturing the covariates $\mathbf{X}_r$ for all the trials $r = 1, \ldots, R$

the VAR model can then be expressed as:

$$\overline{\mathbf{y}}^{(c)} = \overline{\mathbf{X}}\boldsymbol{\omega}^{(c)} + \overline{\boldsymbol{\varepsilon}}^{(c)}, \tag{2}$$

where $\overline{\boldsymbol{\varepsilon}}^{(c)} := [\boldsymbol{\varepsilon}_1^{(c)'}, \boldsymbol{\varepsilon}_2^{(c)'}, \ldots, \boldsymbol{\varepsilon}_R^{(c)'}]' \sim \mathcal{N}(0, \sigma^{(c)2}\mathbf{I})$ is a zero-mean Gaussian noise vector of size RN with variance $\sigma^{(c)2}$, and $\boldsymbol{\omega}^{(c)}$ is a parameter vector accounting for the interactions in the network, for $c = 1, 2, \cdots, C$.

In agreement with the parsing of the covariates in the matrix $\overline{\mathbf{X}}$, the parameter vector $\boldsymbol{\omega}^{(c)} := [\boldsymbol{\omega}^{(c,1)'}, \boldsymbol{\omega}^{(c,2)'}, \ldots, \boldsymbol{\omega}^{(c,C)'}]'$ in Equation 2 is composed of a collection of cross-history dependence vectors $\{\boldsymbol{\omega}^{(c,\tilde{c})}\}^{\tilde{c}=1:C}$, where $\boldsymbol{\omega}^{(c,\tilde{c})}$ represents the contribution of the history of neuron $(\tilde{c})$ to the activity of neuron (c) via the corresponding covariate vector $\mathbf{h}_{r,n}^{(\tilde{c})}$ encoded in matrix $\overline{\mathbf{X}}$. In particular the component $\boldsymbol{\omega}^{(c,c)}$ is important in capturing the slow calcium florescence decay in an autoregressive fashion, and thereby excluding the transient effects of florescence decay from the GC analysis.

Next, we invoke the hypothesis of sparsity in the interactions among the neurons in the ensemble. In our model, the sparsity of the interactions can be captured through the sparsity of the parameter vector $\boldsymbol{\omega}^{(c)}$: when only very few components of $\boldsymbol{\omega}^{(c)}$ are non-zero, neuron (c) is only affected by the activity history of a few neurons in the ensemble. In addition, as the dimension of the parameter vector given by MC scales with the network size C, the hypothesis of sparisty enables the detection of salient interactions within a large network, and thereby mitigates overfitting, especially when the observations are noisy and trials are limited in number.

Parameter Estimation: In order to define a framework for inferring a possible GC link $(\tilde{c} \mapsto c)$, two nested models are taken into account: 1) the VAR model in Equation 2, where the contributing covariates from all the neurons are taken into account, referred to as the full model, and 2) the same model in which the covariates and parameters of a single neuron $(\tilde{c})$ on neuron (c), $\tilde{c} \neq c$ are excluded, to which we refer as the reduced model. The parameters and covariates associated with the reduced model are denoted by $\boldsymbol{\omega}^{(c\backslash\tilde{c})}$ and $\overline{\mathbf{X}}^{\backslash\tilde{c}}$, respectively.

The sparse parameter vector associated with either of the two models can be estimated by solving an ℓ_1-regularized maximum likelihood (ML) problem for each neuron as follows:

$$\widehat{\boldsymbol{\omega}} = \underset{\boldsymbol{\omega}}{\mathbf{argmin}} \left(\frac{1}{2} \| \overline{\mathbf{y}}^{(c)} - \mathbf{X}\boldsymbol{\omega} \|_2^2 + \gamma \| \boldsymbol{\omega} \|_1 \right), \tag{3}$$

where $\mathbf{X}$ takes the two values of $\overline{\mathbf{X}}$ and $\overline{\mathbf{X}}^{\backslash\tilde{c}}$ for the full and reduced models, respectively, the ℓ_1 -norm is defined as $\| \boldsymbol{\omega} \|_1 := \sum_{m=1}^{M} |\omega_m|$, and $\gamma \geq 0$ is a regularization parameter tuning the sparsity level, which can be selected based on analytical results on ℓ_1 -regularized ML problems or via cross-validation. Given the parameter estimate $\widehat{\boldsymbol{\omega}}$, the corresponding variance associated with the model can be computed as $\widehat{\sigma}^2 = 1/NR \| \overline{\mathbf{y}} - \overline{\mathbf{X}}\widehat{\boldsymbol{\omega}} \|_2^2$.

Inference: The conventional measures of GC are based on ML estimates of the VAR parameters, and not the regularized ML as in our case. Hence, we need to modify the GC measure and the corresponding deviance statistics, to account for the estimation bias incurred due to ℓ_1-regularization. This new measure is the static VAR-based counterpart of a similar measure presented in our earlier studies in the context of dynamic sparse point process models (Sheikhattar and Babadi, 2016) To this end, we modify the deviance difference statistic corresponding to the full and reduced models to compensate for the bias incurred due to sparse regularization. The bias can be computed for the full model as $B^{(c)} := \mathbf{g}^{(c)'} \mathbf{H}^{(c)-1} \mathbf{g}^{(c)}$, where $\mathbf{g}^{(c)} := \overline{\mathbf{X}}' (\overline{\mathbf{y}}^{(c)} - \overline{\mathbf{X}}\widehat{\boldsymbol{\omega}}^{(c)}) / \widehat{\sigma}^{(c)2}$ and $\mathbf{H}^{(c)} := -\overline{\mathbf{X}}'\overline{\mathbf{X}} / \widehat{\sigma}^{(c)2}$ are the gradient and Hessian of the log-likelihood function for the Gaussian VAR model of Equation 2, respectively. Similarly, the bias $B^{(c\backslash\tilde{c})}$ for the reduced model can be computed by replacing the matrix of covariates and parameter estimate by $\overline{\mathbf{X}}^{\backslash\tilde{c}}$ and $\widehat{\boldsymbol{\omega}}^{(c\backslash\tilde{c})}$, respectively.

The deviance difference statistic associated with the two nested full and reduced models can be expressed as:

$$\boldsymbol{D}^{(\tilde{\boldsymbol{c}}\mapsto\boldsymbol{c})}\boldsymbol{:}=\boldsymbol{NR}\log\frac{\widehat{\boldsymbol{\sigma}}^{(\boldsymbol{c}\backslash\tilde{\boldsymbol{c}})2}}{\widehat{\boldsymbol{\sigma}}^{(\boldsymbol{c})2}}-\boldsymbol{B}^{(\tilde{\boldsymbol{c}}\mapsto\boldsymbol{c})}, \tag{4}$$

where $B^{(\tilde{c}\mapsto c)}:=B^{(c)}-B^{(c\backslash\tilde{c})}$ denotes the difference of bias terms corresponding to the full and reduced models.

We finally employ the inference framework presented in (Kim et al., 2011; Sheikhattar and Babadi, 2016) to simultaneously test the statistical significance of all possible GC interactions and to control the FDR at a given significance level α. This inference framework integrates an extension of classical results on analysis of deviance, and a multiple hypothesis testing procedure based on the Benjamini-Yekutieli FDR control (Benjamini and Yekutieli, 2001). The weights of the detected links are further characterized using the Youden's J-statistic, which is a summary statistic for quantifying the strength of hypothesis tests. The excitatory or suppressive nature of GC links are determined by the effective sign of estimated cross-history parameters associated with shorter latencies.

To quantify the spread of the distribution of GC-link directions (Figure 5F), we first constructed a circular histogram of the GC-link angles which were computed from MATLAB built-in function atan2. Based on this histogram we used PCA to extract the long and short axes of the eclipse like distributions. Then all the original angles were projected onto the short axis and the resultant dot products (taking absolute values) were compared between ACX fields. The more the values are shifted toward 1, the larger the spread in the short axis, indicating a less 'pointy' distribution.

Pupillometry data analysis

To extract pupil size, each image was first cropped around the eye and the MATLAB built-in function "imfindcircles" was used to determine pupil location and diameter. The pupil size over time was further smoothed with a time window of ~150ms. The onset of micro-dilations was determined by first inverting the trace (flip sign) and using MATLAB built-in function "findpeaks" with a minimum peak prominence of 10μm. Next, we quantified the occurrence of micro-dilation before, during and after tone onset using 1 s windows, to investigate whether micro-dilations were more likely to occur following tone offset. We established confidence interval by shuffling tone onset time and counting the micro-dilation occurrence in reference to the shuffled stimulus onset. We performed such analysis for 10 sets of experiments (n = 9 mice). If a micro-dilation is more likely to occur during any specific time window, then the actual counts should exceed the upper bound of the confidence interval. If the counts are within the confidence interval, then the occurrence of micro-dilations is equally likely to occur before, during or after tone presentation.

Electrophysiological data analysis

Single units were sorted offline using MClust-3.5 package (A. D. Redish et al., http://redishlab.neuroscience.umn.edu/MClust/MClust.html) and KlustaKwik algorithm (K. Harris, http://klustakwik.sourceforge.net). For single unit analysis, we calculated responses as the spike count change within a 500ms window before or after tone onset/offset and used paired t test to determine the response significance for each frequency.